IEEE Sensors Council IEEE Sensors Reviews

Received 2 July 2025; revised 2 August 2025, 23 August 2025, and 4 September 2025; accepted 8 September 2025. Date of publication 18 September 2025; date of current version 22 October 2025. The review of this article was arranged by Associate Editor Christos Michail.

Digital Object Identifier 10.1109/SR.2025.3611970

Demystifying Pulse Compression in Weather Radar

EIICHI YOSHIKAWA [1,2] (Senior Member, IEEE) AND V. CHANDRASEKAR[1] (Fellow, IEEE)

(Tutorial Paper)

[1]Colorado State University, Fort Collins, CO 80523 USA
[2]The University of Osaka, Suita, Osaka 565-0871, Japan

CORRESPONDING AUTHOR: EIICHI YOSHIKAWA (e-mail: eyoshi@colostate.edu).

This research was supported by the US National Science Foundation.

ABSTRACT Pulse compression is a fundamental technique that enables radar systems to transmit long-duration, low-peak-power signals while achieving both power gain and high range resolution. This dual advantage makes pulse compression an essential component of modern radar systems, which demand compactness, lightweight design, and energy efficiency. While pulse compression implementation has been well studied for hard/point target detection, it remains less established for volume target estimation. This article aims to document the similarities and differences in the use of pulse compression for hard target detection and volume target estimation—an area that has not thoroughly been discussed. Specifically, we express pulse compression radar equations and signal-to-noise ratio for both applications, providing a framework for evaluating the benefits of pulse compression. In addition, we aim to bridge the gap between the theoretical formulation of pulse compression and its practical digital implementation. This integration eliminates the need for readers to consult separate documents on pulse compression theory and digital signal processing. Our goal is to enable readers to fully understand and apply pulse compression in practical scenarios. To this end, the main body of this article focuses on key concepts and practical techniques essential for implementation. Detailed mathematical expressions and extended discussions are provided in the Appendixes for a further understanding.

INDEX TERMS Pulse compression, radar, volume target.

I. INTRODUCTION

Conventional radar systems transmit short-duration, single-frequency pulses, where the peak power directly influences the signal-to-noise ratio (SNR) of the received signal, and the pulse duration determines range resolution. However, radio frequency transmitter technology faces inherent limitations in amplifying such short pulses to high peak power levels. Pulse compression technique addresses this limitation by allowing radar systems to transmit long-duration pulses with various modulation schemes instead of short, unmodulated pulses. The echoes of these long pulses are then compressed into short pulses upon reception, resulting in improved SNR and enhanced range resolution [1], [2].

This pulse compression gain enables the use of lower transmit peak power, making it feasible to replace traditional vacuum tube amplifiers—such as magnetrons, klystrons, and traveling wave tubes—with solid-state amplifiers. Unlike vacuum tube amplifiers, which are large, heavy, power-hungry, and lack precision in pulse shaping, solid-state amplifiers offer advantages in size, weight, power efficiency, and waveform accuracy. These benefits have made modern radar systems significantly more compact, lightweight, and energy-efficient, facilitating deployment on various platforms, including aircraft and spacecraft. As a result, pulse compression has become a standard and indispensable technology in radar system design [3], [4], [5], [6], [7], [8], [9], [10], [11], [12], [13], [14], [15], [16], [17], [18], [19], [20], [21].

This article examines the effects of pulse compression, with particular focus on the similarities and differences between hard target detection and volume target estimation, which have yet to be well documented. While the SNR gain from pulse compression benefits both cases, range resolution impacts only for volume target estimation. To elucidate these distinctions, the radar equations for both scenarios—each incorporating the effects of pulse compression—are compared. For volume target estimation, a new quantity, the pulse compression radar system constant, is introduced as a counterpart to the conventional radar system constant used in traditional radar systems. This new constant simplifies the calibration of volume target estimates using a reference hard target.

Furthermore, this article aims to bridge the gap between the theoretical formulation of pulse compression and its practical digital implementation. A specific digital implementation is proposed that is properly normalized to enhance only signal components in received signal without amplifying noise, thereby simplifying the calibration process. Based on this digital framework, several implementation-specific issues—absent in the idealized theory—are identified and examined. Established methods for mitigating these digital-domain challenges are also discussed.

This article begins by introducing the technical concept of pulse compression, explaining how signals are compressed and how pulse compression benefits the radar equation and SNR in both hard target detection and volume target estimation scenarios. Next, the digital implementation of pulse compression is discussed, covering not only the standard approach but also several enhanced methods based on useful preprocessing techniques. The performance characteristics of these implementations are then examined in detail, highlighting common challenges in the digital domain and demonstrating how the preprocessing methods help mitigate them.

The main body of this article presents the fundamental equations necessary for practical implementation of pulse compression, with an emphasis on clarity and accessibility for learners and practitioners. While mathematical content is included to support understanding and application, more detailed theoretical discussions are provided in the Appendixes for readers seeking a deeper or more rigorous treatment.

II. TECHNICAL CONCEPT

To introduce the technical concept of pulse compression, consider a scenario where a radar system detects two targets, as illustrated in Fig. 1. Fig. 1(a) depicts the operation of a conventional radar. It transmits a short-duration, single-frequency pulse that is upconverted to a carrier frequency by a transmitter and radiated into space via an antenna. The transmitted wave impinges on the targets, generating scattered waves that return to the antenna at different times depending on each target's distance. The received signal is then downconverted and digitized by an analog-to-digital converter (ADC). This received signal primarily consists of delayed and scaled replicas of the transmitted waveform. The delay corresponds to the round-trip time of the electromagnetic wave between the radar and each target, satisfying the relationship $r = c\tau/2$, where r is the target range (in m), c is the speed of light (ms^{-1}), and τ is the time delay (s). To resolve two closely spaced targets, the transmit pulse must be short in duration, as shown in the bottom of Fig. 1(a). The scaling of each return depends on factors, such as the target's (back)scattering cross section and range attenuation.

Fig. 1(b) illustrates the case of a pulse compression radar. Unlike conventional radars, it transmits a long-duration, modulated signal—typically using chirp or coded modulation [1], [3], [22]. Due to the extended pulse duration, the received signal contains overlapping replicas from multiple targets, making them indistinguishable in their raw form. Pulse compression processes the received signal to produce responses that are both power-enhanced and temporally compressed, enabling target separation. The basic technique for pulse compression is the matched filter (MF), which performs a cross-correlation between the received signal and a replica of the transmitted signal waveform. As a result, each delayed and scaled replica of the transmitted signal in the received signal is transformed into a delayed and scaled autocorrelation of the transmit waveform. In this sense, a pulse compression radar can be viewed as functionally equivalent to a conventional radar that transmits a waveform identical to the autocorrelation of the original modulated signal.

Let us examine an example of a long-duration, modulated signal and its MF response, as illustrated in Fig. 2. Fig. 2(a) displays the real part and envelope of the transmitted signal, shown as solid and dashed lines, respectively. The envelope is normalized such that its peak value is unity. Duration of the signal is characterized by the effective duration (s), defined as follows:

$$T_e := \frac{\int_0^T |a(t)|^2 \, dt}{\max_t |a(t)|^2} \tag{1}$$

where $a(t)$ denotes the transmitted signal replica as a function of time (s), and T is the pulse repetition interval (PRI) (s) in s. As shown as the dotted line, the transmitted signal envelope is approximated by a rectangular pulse with duration of T_e. Note that (1) can also be used to compute the effective duration for unnormalized signals by including the peak power in the denominator.

Fig. 2(b) shows the power spectrum of the transmitted signal, whose bandwidth is characterized by the effective bandwidth (Hz), defined as

$$B_e := \frac{\left(\int_0^{B_r} p(f)\, df\right)^2}{\int_0^{B_r} p(f)^2\, df} \tag{2}$$

where $p(f)$ denotes the power spectrum as a function of frequency (Hz), and B_r is the receiver bandwidth (Hz). To ensure that the signal passes through the receiver without significant distortion or attenuation, the condition $B_e \leq B_r$ must be satisfied.

Fig. 2(c) presents the MF response of the transmitted signal, where the real part and the envelope are shown by the solid and dashed lines, respectively. The envelope can also be

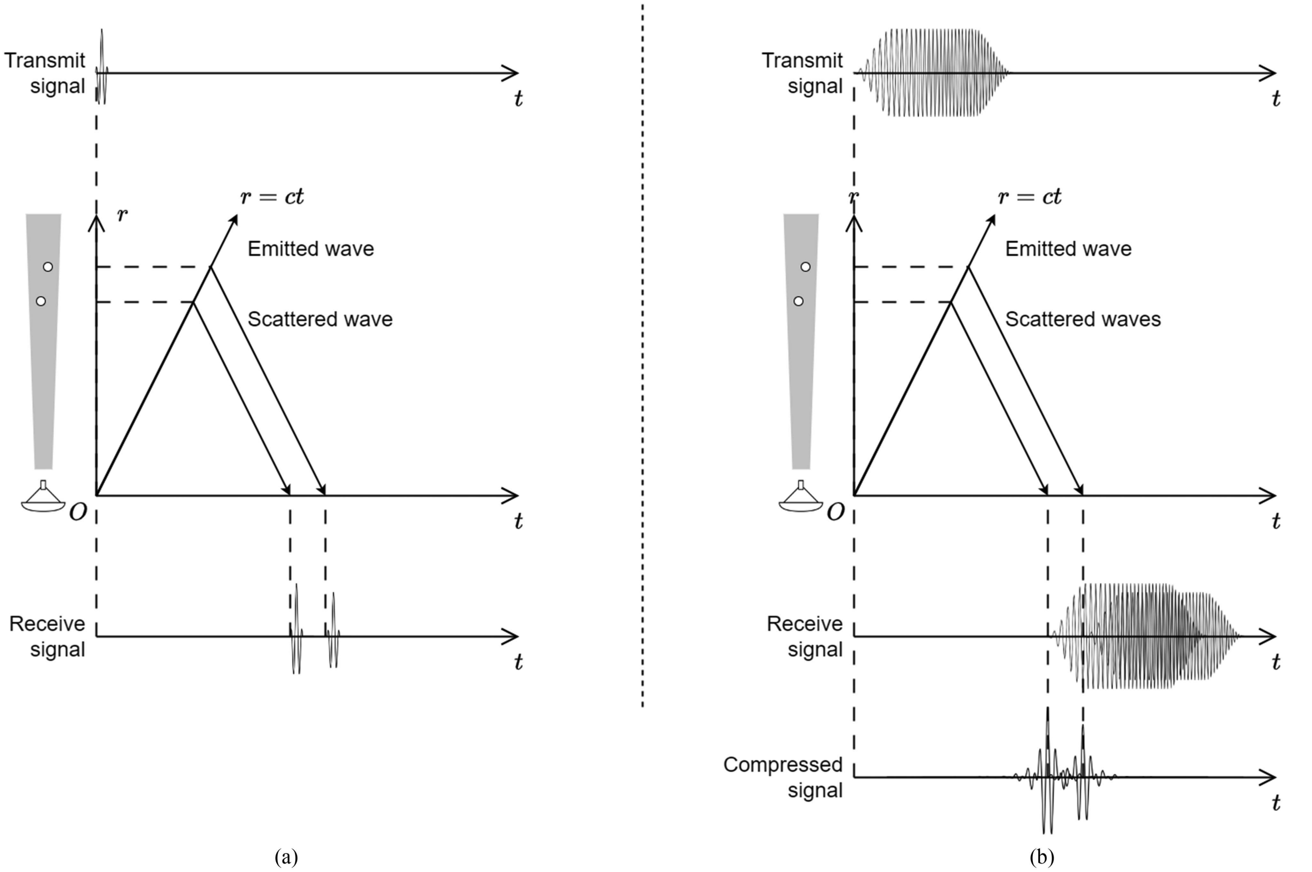

FIGURE 1. Range–time diagrams of radar transmissions and signals for (a) conventional radars and (b) pulse compression radars, illustrating a case with two targets within the radar beam. Conventional radars transmit short-duration, single-frequency pulses and receive echoes that are delayed and scaled replicas of the transmitted signal. A higher peak power and shorter pulse duration improve the detection and separation of targets. In contrast, pulse compression radars transmit long-duration signals modulated in frequency or code, resulting in overlapping echoes from multiple targets in the received signal. The pulse compression processes the received signal to convert these overlapped replicas into sharpened, power-enhanced responses, thereby accomplishing target detectability and separability. (a) Conventional radar; short-duration, signal-frequency pulse. (b) Pulse compression radar; long-duration, modulated pulse.

TABLE 1. Specifications of a Sample Weather Radar System

Item	Value
Transmit peak power	2.4 kW
Antenna gain	45 $\mathrm{dB_i}$
Carrier frequency	5.65 GHz
beamwidth HPBW	1°
System loss	3 dB
Receiver temperature	298 K
Dielectric factor of water	0.925

approximated by a rectangular pulse in the same manner as (1), illustrated by the dotted line. This rectangular approximation has a peak amplitude of $\sqrt{B_r T_e}$ and a duration of $1/B_e$. So, to summarize, pulse compression effectively increases the transmit peak power from P_t to $P_t B_r T_e$ and reduces the signal duration from T_e to $1/B_e$. The resulting gain of $B_r T_e$ applies only to the signal component, not to the noise. As summarized in Table 1, pulse compression enhances the effective transmit peak power from P_t to $P_t B_r T_e$ and compresses the signal duration from T_e to $1/B_e$. The resulting power gain of $B_r T_e$ (or amplitude gain of $\sqrt{B_r T_e}$) applies only to the signal component, not to the noise.

Under the ideal condition where $B_e = B_r$, the power gain can be expressed as $B_e T_e$. In practical scenarios where $B_e < B_r$, the power gain is $B_r T_e$. Since this gain can be increased by enlarging B_r (the receiver bandwidth), it should be regarded as a signal processing gain. As shown in the following section, this amplification cancels out when evaluating the SNR; therefore, it does not represent an improvement in signal quality. For this reason, B_r should only be large enough to ensure accurate signal representation, ideally matching the sampling frequency.

Note that the definitions of effective duration and bandwidth, as well as the approximated peak power and duration of the MF response, follow those presented in [23]. While those definitions are based on continuous formulations, their discrete counterparts are provided in Appendix D. It is also important to distinguish these definitions from other commonly

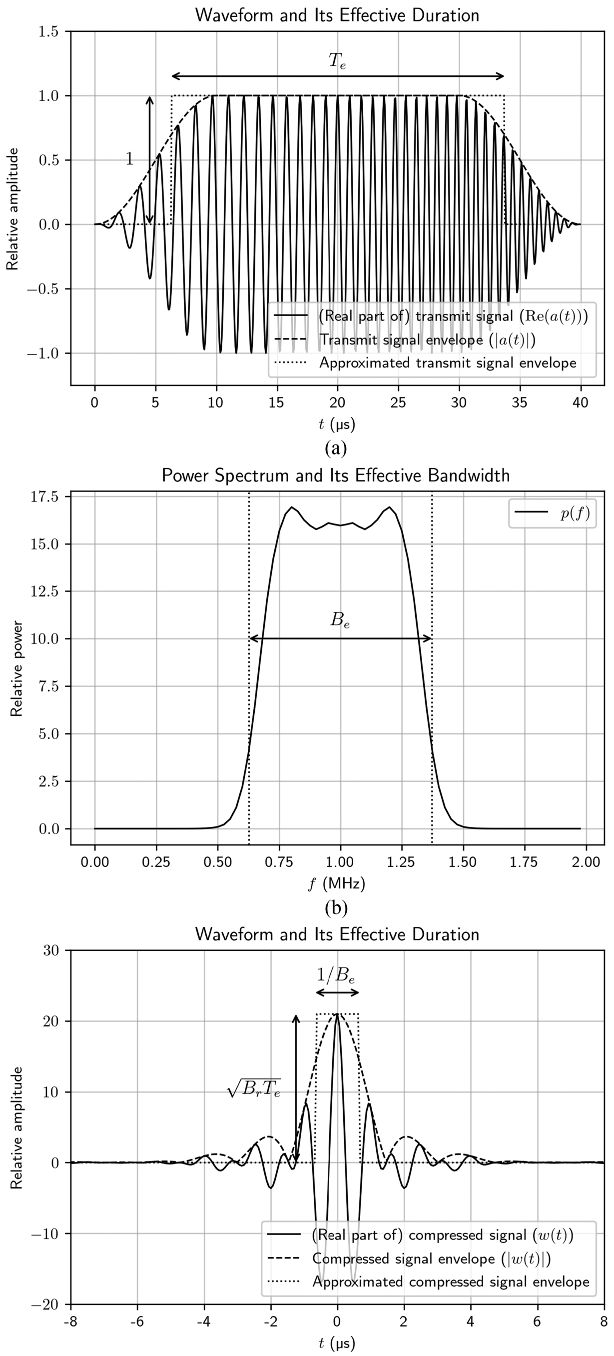

FIGURE 2. Example of (a) a frequency-modulated, long-duration transmitted signal, along with its (b) power spectrum and (c) matched filter (MF) response. In (a), the solid line shows an upchirped signal, while the dashed line indicates its envelope, shaped by a raised-cosine window. The signal's duration is measured using the effective duration defined in (1), corresponding to the width of an energy-equivalent rectangular pulse (shown as a dotted line, also shown as a dashed line). Panel (b) presents the power spectrum of the transmitted signal, whose bandwidth is characterized by the effective bandwidth defined in (2). Panel (c) shows the MF response, with its envelope (dashed) and effective duration (dotted) overlaid. This example illustrates that pulse compression increases the signal's peak amplitude by a factor of $\sqrt{B_r T_e}$ and compresses its duration to $1/B_e$.

used practical measures—such as full-width at half-maximum or the time span between the first and last nonzero points of the signal envelope. The rectangular approximation of both the transmitted signal and the MF response is designed to preserve the total signal energy.

In the following subsections, we examine the benefits of pulse compression from the perspective of radar system performance, focusing specifically on received power, SNR, and dynamic range. These benefits can be quantitatively evaluated using radar equations. Separate formulations of the radar equation are used for hard target detection and volume target estimation, revealing both the similarities and differences in how pulse compression improves performance in each application.

A. RECEIVED POWER

The radar equation is a fundamental tool in radar engineering used to estimate the received power based on radar specifications and target properties. The conventional radar equation for a point target is given by

$$P_r^{(p)} = \frac{P_t G^2 \lambda^2 \sigma^{(p)}}{(4\pi)^3 r^{(p)4} l^{(p)2}} \tag{3}$$

where G is the antenna gain (i.e., the peak level of the antenna directivity), λ is the carrier wavelength (m), $\sigma^{(p)}$ is the backscattering cross section (m^2) of the point target, $r^{(p)}$ is the distance to the point target (m), and $l^{(p)2}$ accounts for power losses along the propagation path and in the radar system. Note that this equation assumes that the target is located on the antenna boresight. A detailed derivation of (3) is provided in Appendix A.

Since (3) does not depend on the effective pulse duration, pulse compression contributes solely through power gain. The radar equation is therefore modified under pulse compression as

$$P_c^{(p)} := B_r T_e P_r^{(p)} = \frac{P_t B_r T_e G^2 \lambda^2 \sigma^{(p)}}{(4\pi)^3 r^{(p)4} l^{(p)2}} \tag{4}$$

which we refer to as the *pulse compression radar equation for a point target*. $P_c^{(p)}$ is a compressed power for a hard target.

In contrast, the conventional radar equation for a volume target is given by

$$P_r^{(v)} \approx \frac{P_t G^2 \lambda^2 c T_e \theta_h^2}{2^{10} (\ln 2) \pi^2 r^{(v)2} l^{(v)2}} \eta \tag{5}$$

where $r^{(v)}$ and $l^{(v)}$ are the range (m) and power losses to the volume target, respectively. θ_h is the half-power (-3 dB) beamwidth of the antenna in radians, and η is the backscattering cross section per unit volume (m^2 m^{-3}), also known as reflectivity. A detailed derivation of (5) is also provided in Appendix A. Notice that T_e and θ_h determine the effective resolution volume. Equation (5) is often written in a simplified form

$$P_r^{(v)} \approx \frac{C}{r^{(v)2}} \eta \tag{6}$$

where the radar system constant C is defined as

$$C := \frac{P_t G^2 \lambda^2 c T_e \theta_h^2}{2^{10}(\ln 2)\pi^2 l^{(v)2}}. \quad (7)$$

Because (5) includes both P_t and T_e, it is affected by both the power gain and pulse duration compression provided by pulse compression. This results in an effective gain of $B_r T_e/(B_e T_e) = B_r/B_e$, leading to the *pulse compression radar equation for a volume target* as

$$P_c^{(v)} = \frac{B_r}{B_e} P_r^{(v)} \approx \frac{B_r}{B_e} \frac{P_t G^2 \lambda^2 c T_e \theta_h^2}{2^{10}(\ln 2)\pi^2 r^{(v)2} l^{(v)2}} \eta \quad (8)$$

where $P_c^{(v)}$ is a compressed power for a volume target. Similarly to (5), this can be written in the simplified form as

$$P_c^{(v)} \approx \frac{C_c}{r^{(v)2}} \eta \quad (9)$$

where the *pulse compression radar system constant* C_c is defined as

$$C_c := \frac{B_r}{B_e} C = \frac{B_r}{B_e} \frac{P_t G^2 \lambda^2 c T_e \theta_h^2}{2^{10}(\ln 2)\pi^2 l^{(v)2}}. \quad (10)$$

These equations highlight the different benefits of pulse compression in each scenario: $P_c^{(p)} \propto B_r T_e$ and $P_c^{(v)} \propto B_r/B_e$. Pulse compression does not provide a power gain for volume target estimation as great as hard target detection because increasing the effective bandwidth narrows the resolution volume, thereby reducing the total backscattered power from a volume target.

As discussed in [24] for conventional radars, the pulse compression radar equations in (4) and (8) enable calibration of the pulse compression radar system constant using a known reference hard target, such as a metal sphere. The ratio of received powers from a volume target and the reference sphere derives

$$P_c^{(v)} \approx \frac{C_c'}{r^{(v)2}} \eta \quad (11)$$

where C_c' is the calibrated pulse compression radar system constant, given by

$$C_c' = \frac{P_c^{(r)}\, c\,(1/B_e)\,\theta_h^2\, \pi\, r^{(r)4}\, l^{(p)2}}{2^4 (\ln 2)\, \sigma^{(r)}\, l^{(v)2}} \quad (12)$$

in which $P_c^{(r)}$ is the received power from the reference hard target after pulse compression, $r^{(r)}$ is its range (m), and $\sigma^{(r)}$ is its backscattering cross section (m^2). For a metal sphere whose diameter is sufficiently larger than the radar carrier wavelength λ, the backscattering cross section $\sigma^{(r)}$ closely approximates its geometric cross section [25].

B. SIGNAL-TO-NOISE RATIO (SNR)

Since the power gain from pulse compression does not apply to noise, the SNRs for both applications are obtained by dividing the received power by the system noise power (W) defined as $P_n := k_B \mathcal{T} B_r$, where k_B is the Boltzmann constant

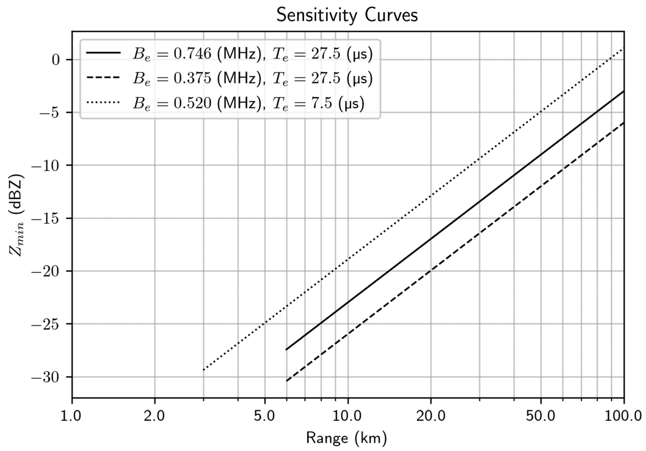

FIGURE 3. Radar sensitivity curves computed for various combinations of B_e and T_e, which are pulse compression parameters affecting the SNR for volume target estimation. As indicated by (14) and (15), the minimum detectable reflectivity factor decreases (i.e., sensitivity improves) with increasing T_e or decreasing B_e.

(JK^{-1}) and $\mathcal{T}$ is the system noise temperature (K). Here, it is assumed that other noise sources, such as antenna-received external noise, are negligible compared to the system noise. Accordingly, the SNR for hard target detection is given by

$$\Pi_c^{(p)} = \frac{P_t T_e G^2 \lambda^2 \sigma^{(p)}}{(4\pi)^3 r^{(p)4} l^{(p)2} k_B \mathcal{T}} \quad (13)$$

where the gain factor B_r cancels out. On the other hand, the SNR for volume target estimation is

$$\Pi_c^{(v)} \approx \frac{P_t G^2 \lambda^2 c T_e \theta_h^2}{2^{10}(\ln 2)\pi^2 r^{(v)2} l^{(v)2} k_B \mathcal{T} B_e} \eta. \quad (14)$$

It is important to examine how the pulse compression parameters B_r, T_e, and B_e contribute to $\Pi_c^{(p)}$ and $\Pi_c^{(v)}$. Specifically, $\Pi_c^{(p)} \propto T_e$ and $\Pi_c^{(v)} \propto T_e/B_e$, indicating that pulse compression provides greater SNR improvement for hard target detection than for volume target estimation. It is also important to note that neither SNR expression depends on the receiver bandwidth B_r. This reflects the fact that while B_r determines the system noise power P_n, it is effectively canceled out by the pulse compression gain. While the SNR for a hard target detection does not depend on B_r, in volume target estimation, the effective bandwidth B_e, rather than B_r, determines the noise power contribution in pulse compression systems.

For volume target estimation, if the minimum detectable reflectivity $\eta_{\min}(r)$ corresponds to the threshold $\Pi_c^{(v)} = 1$, then the radar sensitivity is given by

$$\eta_{\min}(r) = \frac{r^2 P_n}{C_c} \propto \frac{B_e}{T_e} \quad (15)$$

which clearly shows that smaller B_e or larger T_e improves sensitivity.

Fig. 3 illustrates sensitivity curves calculated using realistic radar parameters listed in Table 1. The minimum reflectivity factor $Z_{\min}$ (dBZ) is computed from $\eta_{\min} = (\pi^5/\lambda^4)|K_w|^2 z_{\min}$ and $Z_{\min} = 10\log_{10}(z_{\min} \times 10^{18})$ where $z_{\min}$ is the minimum reflectivity factor in the linear scale (mm ^{6} m^{-3}), and $|K_w|^2$ is the dielectric factor of water [26]. The solid, dashed, and dotted curves represent, respectively, the following pulse parameters:

1) $B_e = 0.746\,\text{MHz}$, $T_e = 27.5\,\mu s \rightarrow$ resolution: 201 m;
2) $B_e = 0.375\,\text{MHz}$, $T_e = 27.5\,\mu s \rightarrow$ resolution: 400 m;
3) $B_e = 0.520\,\text{MHz}$, $T_e = 7.5\,\mu s \rightarrow$ resolution: 288 m.

This comparison confirms that increasing T_e or reducing B_e (degrading range resolution) yields improved sensitivity (i.e., a lower minimum detectable reflectivity), consistent with (14) and (15) ($z_{\min} \propto \eta_{\min} \propto B_e/T_e$). However, as shown in the figure, a longer pulse duration also introduces a drawback: the initial range becomes unobservable, a limitation that will be discussed further in the next section.

C. DYNAMIC RANGE

The dynamic range of a radar receiver is defined as the difference between the minimum and maximum receivable power levels. If the input power exceeds the receiver's maximum input threshold, the signal becomes saturated, resulting in nonlinear distortion that prevents accurate signal analysis. Thus, radars are typically designed to ensure that received signals remain within the dynamic range. At the same time, radar systems must handle both strong echoes from nearby targets and weak echoes from distant ones—signals that can differ in power by orders of magnitude. Dynamic range is therefore one of the critical performance specifications in radar design [5].

Pulse compression enhances the dynamic range because its gain is realized after the digitization, not raising the analog front-end requirements. For hard target detection, the improvement in dynamic range can be quantified by the ratio of pulse-compressed power to conventional received power as

$$\frac{P_c^{(p)}}{P_r^{(p)}} = B_r T_e. \tag{16}$$

For volume target estimation, the improvement is given by

$$\frac{P_c^{(v)}}{P_r'^{(v)}} \approx \frac{B_r T_e}{B_e T_e'} \tag{17}$$

where $P_r'^{(v)}$ is defined as

$$P_r'^{(v)} := \frac{P_t G^2 \lambda^2 c T_e' \theta_h^2}{2^{10}(\ln 2)\pi^2 r^{(v)2} l^{(v)2}}\eta. \tag{18}$$

This expression is similar to $P_r^{(v)}$ [see (5)], except that T_e is replaced by T_e', representing the temporal duration over which the strong reflectivity is concentrated. It is assumed here that this high-reflectivity region is narrower than the effective pulse duration, i.e., $T_e' < T_e$. We also assume that the reflectivity is approximately uniform within the region. Equations (16) and (17) together indicate that the improvement in volume target estimation is typically less compared with hard target detection, since the condition $B_e T_e' > 1$ is commonly encountered.

As an illustrative example, consider a case where a region of intense reflectivity spans 1 km in range, corresponding to $T_e' = 6.67\,\mu$s. If $B_r = 2\,\text{MHz}$, $B_e = 1\,\text{MHz}$, and $T_e = 27.5\,\mu$s, then the dynamic range improvements due to pulse compression are approximately 17.40 dB for hard target detection and 9.16 dB for volume target estimation.

III. IMPLEMENTATION

MF, the fundamental technique for pulse compression, computes the cross-correlation between the received signal and a normalized replica of the transmitted signal. Its digital implementation is given by

$$\mathbf{z} = \frac{1}{\sqrt{\boldsymbol{\alpha}^{\mathrm{H}}\boldsymbol{\alpha}}}\mathbf{C}^{\mathrm{H}}\mathbf{y} \tag{19}$$

where $\mathbf{y}$ is the complex-valued, discretized received signal. Such signals are typically obtained from receivers equipped with an IQ demodulator followed by two ADCs—one for the in-phase (I) channel and the other for the quadrature (Q) channel. Alternatively, receivers with a single ADC must sample at twice the rate and output real-valued signals, which can be converted to complex form using a method described in Appendix B. The vector $\boldsymbol{\alpha}$ is the transmitted signal replica followed by zeros to match the length of $\mathbf{y}$, and $\mathbf{C}$ is a circulant matrix whose first column is $\boldsymbol{\alpha}$. The superscript $\cdot^{\mathrm{H}}$ indicates the conjugate transpose (Hermitian transpose). The resulting $\mathbf{z}$ is the matched-filtered (compressed) signal and can be interpreted as an estimated (complex) range profile.

MF can be efficiently computed using the Fourier decomposition of the circulant matrix as

$$\mathbf{z} = \frac{1}{\sqrt{\boldsymbol{\alpha}^{\mathrm{H}}\boldsymbol{\alpha}}}\mathbf{F}^{\mathrm{H}}\mathrm{diag}\left(\sqrt{\mathrm{length}(\boldsymbol{\alpha})}\mathbf{F}\boldsymbol{\alpha}\right)^*\mathbf{F}\mathbf{y} \tag{20}$$

where $\mathbf{F}$ denotes the Fourier matrix. The superscript $\cdot^*$ denotes the complex conjugation operation. This expression allows for a fast algorithm as follows.

1) Precompute $\mathbf{s}_\alpha = \mathrm{DFT}(\boldsymbol{\alpha})^*/\sqrt{\boldsymbol{\alpha}^{\mathrm{H}}\boldsymbol{\alpha}}$.
2) Compute $\mathbf{s}_y = \mathrm{DFT}(\mathbf{y})$.
3) Perform element-wise multiplication: $\mathbf{s}_z = \mathbf{s}_y \circ \mathbf{s}_\alpha$.
4) Compute $\mathbf{z} = \mathrm{IDFT}(\mathbf{s}_z)$.

Here, DFT$(\cdot)$ and IDFT$(\cdot)$ denote the discrete Fourier transform (DFT) and inverse discrete Fourier transform (IDFT), respectively. In this article, we adopt the conventional normalization convention: the DFT is unnormalized, while the IDFT includes a $1/\mathrm{length}(\cdot)$ scaling factor. The symbol $\circ$ represents elementwise (Hadamard) multiplication. Note that Step 1 can be precomputed offline, prior to real-time processing.

While some radars store the entire received signal over the PRI [3], [9], most discard the initial M samples of $\mathbf{y}$, where M corresponds to the number of samples in the transmitted signal. This is because these samples are often saturated due to direct leakage from the transmitter. In such cases, $\mathbf{y}$ is defined as $\mathbf{y} = \begin{bmatrix} y_M & y_{M+1} & \cdots & y_n & \cdots & y_{N-1} \end{bmatrix}^{\mathrm{T}}$, where the subscript n corresponds to a delay time of $n\delta_t$, with δ_t

being the sampling interval (s). The total number of samples in a PRI is N, satisfying $N\delta_t = T$. Truncating $\mathbf{y}$ in this way results in a compressed signal $\mathbf{z}$ given by $\mathbf{z} = \begin{bmatrix} z_M & z_{M+1} & \cdots & z_{\hat{i}} & \cdots & z_{N-1} \end{bmatrix}^{\mathrm{T}}$, where the subscript $\hat{i}$ also corresponds to the delay time, $\hat{i}\delta_t$. To interpret $\mathbf{z}$ as a range profile, each delay index $\hat{i}$ can be mapped to a physical range via $\hat{i}\delta_r$, where $\delta_r := c\delta_t/2$.

The following subsections present two additional preprocessing methods: one method retrieves the initial M samples of the compressed signal, and the other enhances the range sampling resolution to produce a finer range profile. These approaches can also be combined to take advantage of both capabilities.

A. ZERO PADDING

Zero padding is a standard technique in digital signal processing [27], commonly used to mitigate issues arising from the periodicity assumption of the DFT. In the context of weather radar, the authors in [28] and [29] proposed a variation—"prepending" zeros (rather than appending) to the received signal—in order to recover the initial M samples of the compressed signal that are typically lost due to saturation. This preprocessing technique is referred to as zero-padding pulse compression in this article. When applied to MF, we refer to it as zero-padding matched filter (ZMF). The ZMF operation is expressed as

$$\mathbf{z}_z = \frac{1}{\sqrt{\boldsymbol{\alpha}_z^{\mathrm{H}}\boldsymbol{\alpha}_z}}\mathbf{C}_z\mathbf{y}_z \tag{21}$$

where $\mathbf{y}_z$ is the received signal with M prepended zeros as $\mathbf{y}_z := \begin{bmatrix} \mathbf{0}_M^{\mathrm{T}} & \mathbf{y}^{\mathrm{T}} \end{bmatrix}^{\mathrm{T}}$. Thus, $\mathbf{y}_z$ is an N-vector, as illustrated in Fig. 4(b). Compared to $\mathbf{y}$ (the received signal for MF, shown in Fig. 4(a), the vector $\mathbf{y}_z$ contains M leading zeros (e.g., $M = 80$ in the example). $\mathbf{C}_z$ is a circulant matrix whose first column is $\boldsymbol{\alpha}_z$, an N-length vector composed of the transmitted signal replica followed by $N - M$ zeros. The resulting compressed signal is denoted by $\mathbf{z}_z := \begin{bmatrix} z_0 & z_1 & \cdots & z_{N-1} \end{bmatrix}^{\mathrm{T}}$, with delay times ranging from 0 to $(N-1)\delta_t$, corresponding to physical ranges from 0 to $(N-1)\delta_r$.

It should be noted that the gain and effective range resolution of the initial M samples in $\mathbf{z}_z$ differ from those of the remaining samples, as will be discussed later.

Since (21) shares the same structure as (19), the fast MF algorithm can also be applied to ZMF by substituting $\mathbf{y}$ and $\boldsymbol{\alpha}$ with $\mathbf{y}_z$ and $\boldsymbol{\alpha}_z$, respectively. Furthermore, additional zeros may be appended to $\mathbf{y}_z$ to make its length a power of two, which enables efficient computation via the fast Fourier transform (FFT). In such cases, the samples of $\mathbf{z}_z$ beyond index $N-1$ are identically zero.

B. UPSAMPLING

Upsampling is another well-known technique in digital signal processing [30], which increases the sampling rate of a signal

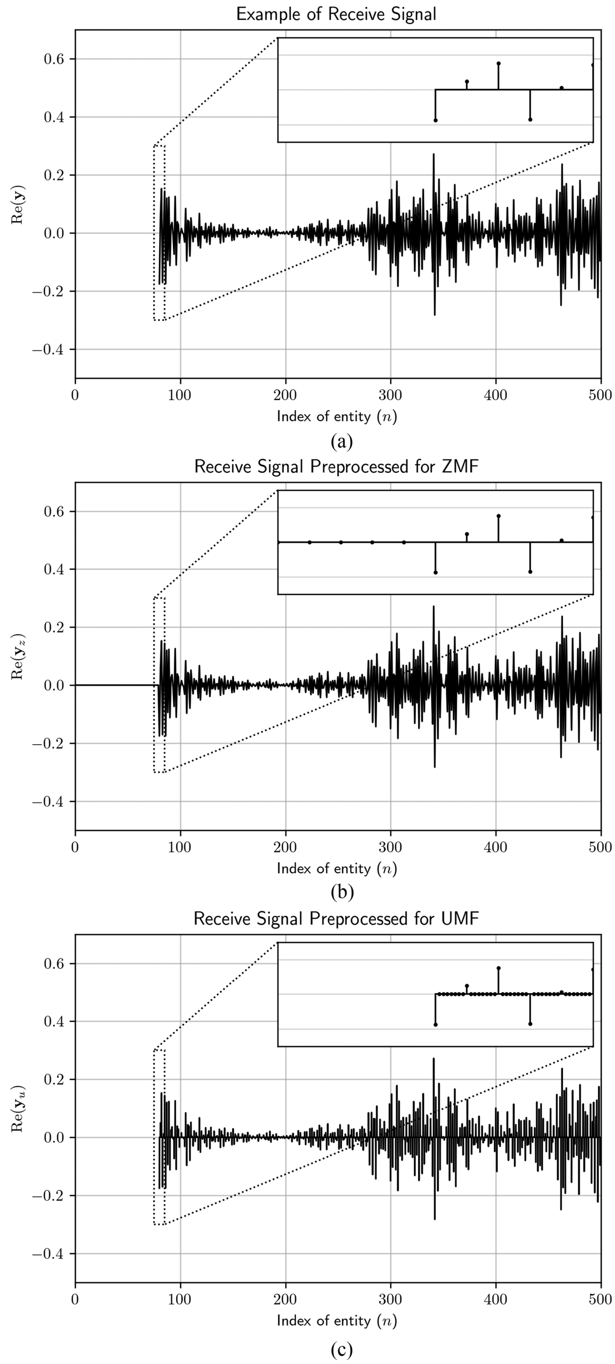

FIGURE 4. Example of a received signal to be processed by the matched filter (MF), along with versions used for Zero-padding and Upsampling MF (ZMF and UMF, respectively). (a) Original signal y for MF, with indices ranging from $n = M$ (= 80) to $n = N - 1$ (N = 500). The initial M samples are truncated under the assumption that they are distorted by receiver saturation. Due to this truncation, MF cannot retrieve the first M range bins of the range profile. (b) Zero-padded version $\mathbf{y}_z$, in which M zeros are prepended. ZMF applies matched filtering to $\mathbf{y}_z$, enabling recovery of the initial M range bins. However, as discussed in the following section, the gain and resolution in these bins differ from those in the other region. (c) Upsampled version $\mathbf{y}_u$, created by inserting zeros between adjacent samples of the original received signal. UMF performs matched filtering on $\mathbf{y}_u$, achieving retrievals with higher range sampling rate. The improved range sampling rate is referred to as display range resolution which is different from range resolution. These two preprocessing techniques can be combined to gain the benefits of both zero-padding and upsampling.

by an integer factor. In the radar context, this enables a finer sampling of the compressed signal in the range domain. We refer to pulse compression with upsampling as upsampled pulse compression, and the corresponding MF implementation as upsampled matched filter (UMF). UMF is expressed as

$$\mathbf{z}_u = \sqrt{\frac{U}{\boldsymbol{\alpha}_u^{\mathrm{H}}\boldsymbol{\alpha}_u}}\mathbf{C}_u\mathbf{y}_u \tag{22}$$

where $\mathbf{y}_u$ is constructed by inserting $U-1$ zeros, $\mathbf{0}_u$, between each sample of $\mathbf{y}$ as $\mathbf{y}_u = \begin{bmatrix} y_M & \mathbf{0}_u^{\mathrm{T}} & y_{M+1} & \mathbf{0}_u^{\mathrm{T}} & \cdots & y_{N-1} & \mathbf{0}_u^{\mathrm{T}} \end{bmatrix}^{\mathrm{T}}$. Now, the total number of samples in $\mathbf{y}_u$ becomes $U(N-M)$. Fig. 4(c) shows an example for $U=8$. The circulant matrix $\mathbf{C}_u$ is constructed from the column vector $\boldsymbol{\alpha}_u$, which is the oversampled version of the transmitted signal, sampled at U times the original rate. Unlike $\mathbf{y}_u$, which is formed by zero-insertion, $\boldsymbol{\alpha}_u$ is generated directly from the higher rate sampled transmitted signal without interpolation or padding. The resulting upsampled compressed signal $\mathbf{z}_u$ is defined as $\mathbf{z}_u = \begin{bmatrix} z_M & z_{M+1/U} & \cdots & z_{N-1+(U-1)/U} \end{bmatrix}^{\mathrm{T}}$, providing a range profile sampled at intervals of δ_r/U. This interval is referred to as display range resolution (m).

Note that while UMF improves the visual granularity of the range profile (i.e., the display range resolution), it does not improve the actual range resolution, as discussed in the following section.

As with ZMF, the fast MF algorithm can also be applied to UMF by replacing the corresponding vectors and matrices with their upsampled counterparts.

IV. DIGITAL IMPLEMENTATION ISSUES

This section analyzes the compressed signals obtained from the MF, ZMF, and UMF. The results demonstrate that the benefits of pulse compression are preserved in practical digital implementations, while also revealing inherent implementation-specific issues. The analysis is based on the following radar-received signal model

$$\mathbf{y} = \mathbf{A}\mathbf{x} + \mathbf{n} \tag{23}$$

where $\mathbf{x} := \begin{bmatrix} x_1 & x_2 & \cdots & x_i & \cdots & x_{N-1} \end{bmatrix}^{\mathrm{T}}$ denotes an inherent complex range profile of an observed scene. The index i corresponds to the range $i\delta_r$ (m). The value at $i=0$ (zero-delay) is omitted from $\mathbf{x}$ due to the received-signal truncation. We can assume $\mathbf{x}$ follows a complex Gaussian distribution as $\mathbf{x} \sim \mathcal{CN}(\mathbf{0}, \mathrm{diag}(\boldsymbol{\sigma}_x^2))$, where $\boldsymbol{\sigma}_x^2 := \begin{bmatrix} \sigma_{x_1}^2 & \sigma_{x_2}^2 & \cdots & \sigma_{x_{N-1}}^2 \end{bmatrix}^{\mathrm{T}}$ represents range-dependent power levels. $\mathbf{n}$ is additive noise modeled as zero-mean complex Gaussian: $\mathbf{n} \sim \mathcal{CN}(\mathbf{0}, \sigma_n^2\mathbf{I})$, which can be approximately assumed with a condition of $B_r \approx 1/\delta_t$. The matrix $\mathbf{A}$ is a truncated Toeplitz matrix, as illustrated in Fig. 5, with dimensions $(N-M)\times(N-1)$. Its columns includes vertically shifted and truncated versions of the transmitted signal $\mathbf{a} := \begin{bmatrix} a_0 & a_1 & \cdots & a_{M-1} \end{bmatrix}^{\mathrm{T}}$, such that the first column includes only a_{M-1}, and the last column includes only a_0. See Appendix C for further details on the radar-received signal formulation.

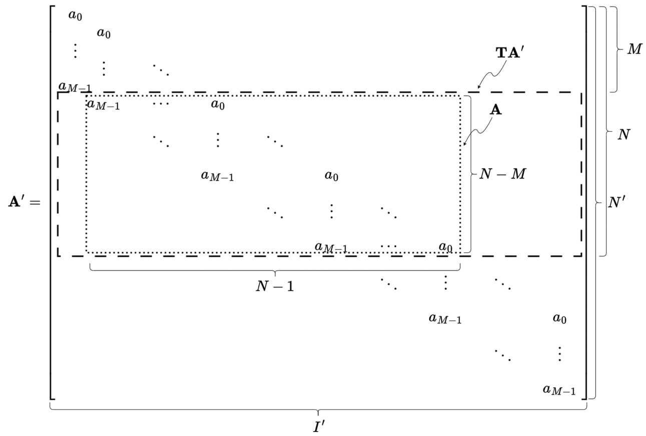

FIGURE 5. Description of the matrix A in the radar-received signal model, highlighted by the dotted square. The matrix A is obtained by truncating a Toeplitz matrix A′, whose first column consists of the power-normalized transmitted signal replica a followed by zeros. The top and bottom rows of A′ are removed due to truncation of the received signal y, caused by receiver saturation and PRI segmentation, respectively, resulting in TA′ (the dashed square). The leftmost and rightmost columns of TA′ are also discarded because they contain only zeros. Further details on the radar-received signal model and the construction of A are provided in Appendix C.

Substituting (23) into the MF formulation in (19), we obtain

$$\mathbf{z} = \hat{\mathbf{x}} + \hat{\mathbf{n}} \tag{24}$$

where $\hat{\mathbf{x}} := \begin{bmatrix} \hat{x}_M & \cdots & \hat{x}_{N-1} \end{bmatrix}$ and $\hat{\mathbf{n}} := \begin{bmatrix} \hat{n}_M & \cdots & \hat{n}_{N-1} \end{bmatrix}$ denote the signal and noise components of $\mathbf{z}$, respectively. The signal component is given by

$$\hat{\mathbf{x}} := \mathbf{W}^{\mathrm{H}}\mathbf{x} \tag{25}$$

where

$$\mathbf{W}^{\mathrm{H}} := \frac{1}{\sqrt{\boldsymbol{\alpha}^{\mathrm{H}}\boldsymbol{\alpha}}}\mathbf{C}^{\mathrm{H}}\mathbf{A}. \tag{26}$$

Here, $\mathbf{W}$ is an $(N-1)\times(N-M)$ matrix. Focusing on the $\hat{i}$th element of the retrieved range profile, we write

$$\hat{x}_{\hat{i}} = \mathbf{w}_{\hat{i}}^{\mathrm{H}}\mathbf{x} \tag{27}$$

where $\mathbf{w}_{\hat{i}}$ is the $\hat{i}$th column of $\mathbf{W}$, referred to as the MF response at range bin $\hat{i}$. Thus, $\hat{x}_{\hat{i}}$ is a weighted average of $\mathbf{x}$, and the peak amplitude and sharpness of $\mathbf{w}_{\hat{i}}$ correspond to the gain and range resolution, respectively.

The noise component is expressed as

$$\hat{\mathbf{n}} = \frac{1}{\sqrt{\boldsymbol{\alpha}^{\mathrm{H}}\boldsymbol{\alpha}}}\mathbf{C}^{\mathrm{H}}\mathbf{n} \tag{28}$$

which preserves the noise power as $\mathrm{E}[|\hat{n}_{\hat{i}}|^2] = \sigma_n^2$ (see its derivation in Appendix D), which indicates that the definition of pulse compression [see (19)] does not gain the noise power level by the normalization factor of $1/\sqrt{\boldsymbol{\alpha}^{\mathrm{H}}\boldsymbol{\alpha}}$.

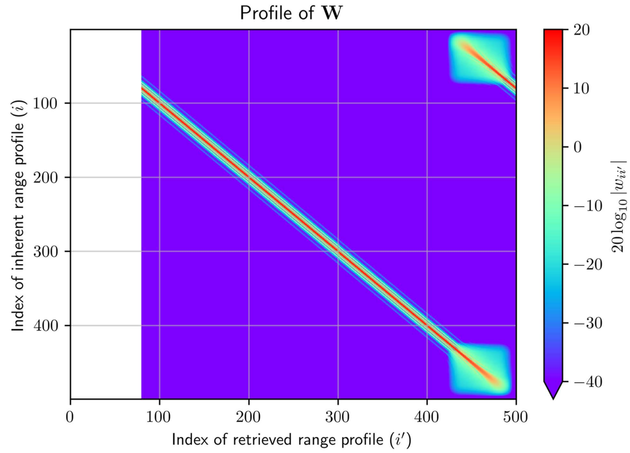

(a)

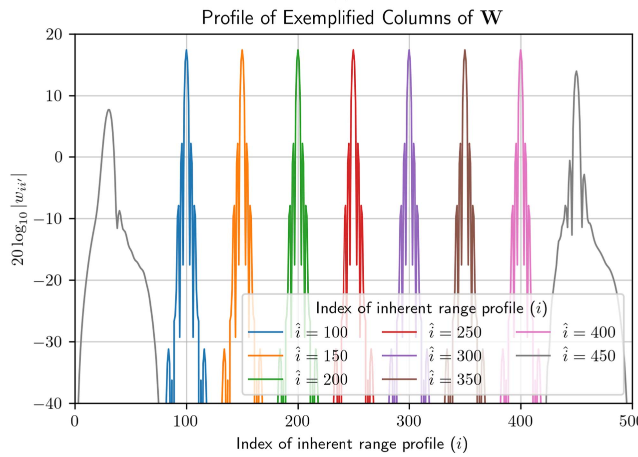

(b)

FIGURE 6. **An example of W containing matched filter (MF) responses across all range bins. (a) Full set of MF responses, with the horizontal axis representing the indices of the retrieved range profile, $\hat{i}$. Each column of W corresponds to an MF response which is as a function of the inherent range profile index i on the vertical axis. (b) Eight selected MF responses to provide a clearer view of individual waveform shapes.**

Fig. 6(a) shows all MF responses contained in $\mathbf{W}$, assuming the transmitted signal waveform in Fig. 2(a). Selected responses are plotted in Fig. 6(b). Between $\hat{i} = M$ $(= 80)$ and $N - M$ $(= 420)$, the MF responses are well-shaped and consistent. Outside this region (i.e., $\hat{i} > N - M$), responses degrade—exhibiting reduced gain, poorer resolution, and larger sidelobes—due to the circulant nature of $\mathbf{C}$.

Gain and range resolution for $\hat{x}_{\hat{i}}$ are defined as

$$g_{\hat{i}} := \max_{i} |w_{i\hat{i}}|^2 \tag{29}$$

and

$$\Delta_{\hat{i}} := \frac{\sum_i |w_{i\hat{i}}|^2}{g_{\hat{i}}}. \tag{30}$$

These definitions follow [23]. For their derivations, see Appendix D. The unitless number $\Delta_{\hat{i}}$ is converted to meters via $\delta_r \Delta_{\hat{i}}$. Fig. 7 plots gain and range resolution as functions of $\hat{i}$. From M to $N - M$, both values are constant: 17.4 dB for gain and 201 m for range resolution. These correspond to $B_r T_e$ and $1/B_e$, respectively. For the transmitted signal waveform in Fig. 2(a), $B_r = 2$ MHz, $T_e = 27.5$ μs, and $B_e = 0.746$ MHz.

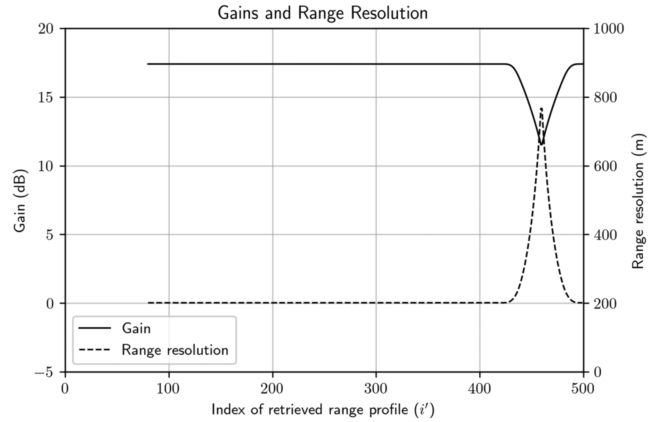

FIGURE 7. **Gain and range resolution of the matched filter (MF), computed using (29) and (30), respectively. The digital implementation yields a gain of 17.4 dB and a range resolution of 201 m, consistent with the theoretical values of $B_r T_e$ and $1/B_e$. These values are based on the transmitted waveform shown in Fig. 2, with parameters $B_r = 2$ MHz, $T_e = 27.5$ μs, and $B_e = 0.746$ MHz. Note that the performance degrades near the trailing edge of the retrieved range profile due to the circulant structure of the MF.**

ZMF are evaluated in the same manner. Fig. 8(a) presents the full set of ZMF responses for the same transmit waveform. Examples in Fig. 8(b) show that ZMF enables retrieval of $\hat{x}_{\hat{i}}$ for $\hat{i} = 1$ to $M - 1$ $(= 79)$. These responses are single-peaked but still inferior to the main region. In Fig. 9, both gain and resolution match the MF between $\hat{i} = M$ and $N - M$, but significantly degrade near the edges. This edge degradation, however, does not occur in radar systems that do not apply the truncation [3], [9], [31].

Responses of UMF are shown in Fig. 10(a) and (b). Results in Fig. 11 indicate that UMF achieves identical gain and resolution as MF but provides finer display resolution. It is tempting to improve display resolution via interpolation of MF outputs. However, this is fundamentally different from UMF. For instance, linear interpolation between $z_{\hat{i}}$ and $z_{\hat{i}+1}$, which is specifically $v z_{\hat{i}} + (1 - v) z_{\hat{i}+1}$ for $0 \le v \le 1$, is equivalent to applying a weighting function as $(v\mathbf{w}_{\hat{i}} + (1 - v)\mathbf{w}_{\hat{i}+1})^{\mathrm{H}}\mathbf{x}$. As shown in Fig. 12, this leads to poorer performance—lower gain, degraded resolution, and possible double peaks—compared to UMF.

V. DISCUSSION

A. DOPPLER EFFECT

Doppler effects reduce the correlation between transmitted and received signals, leading to degraded pulse compression performance, such as gain loss and degraded range resolution. In weather radar applications, however, target radial velocities are relatively low for typical carrier frequencies in the S-, C-, and X-bands, the impact of Doppler is generally negligible. Linear chirp waveforms, in particular, are known for their robustness to Doppler shifts. Nevertheless, Doppler effects

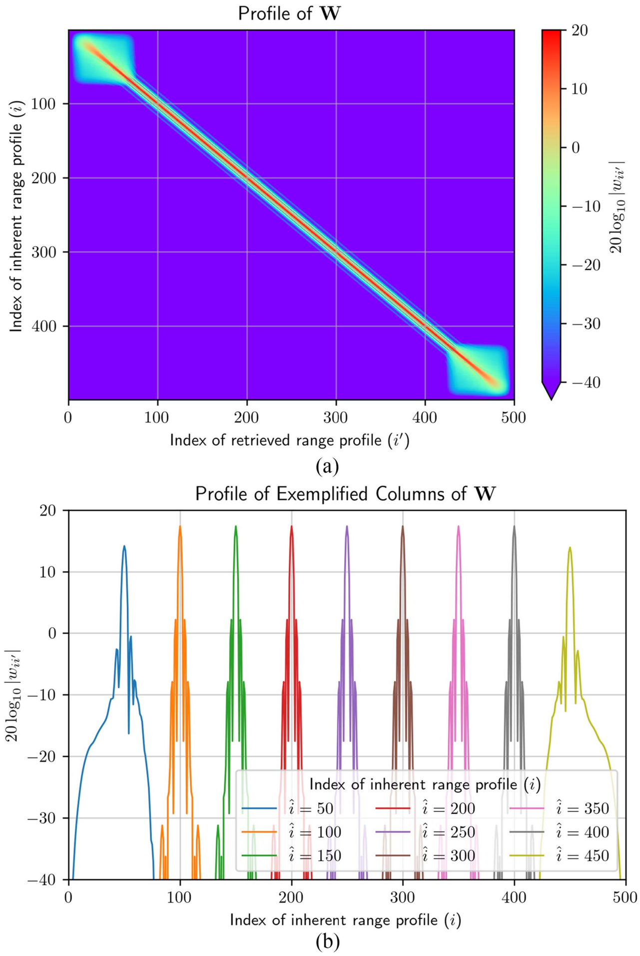

FIGURE 8. **Example of W containing ZMF responses across all range bins. This figure is analogous to the one for standard MF (see Fig. 6), but here W is obtained using ZMF instead. (a) ZMF responses, with the horizontal axis representing indices of the retrieved range profile, $\hat{i}$. Each column corresponds to a ZMF response as a function of the inherent range profile index i. (b) Eight selected responses for clearer visualization.**

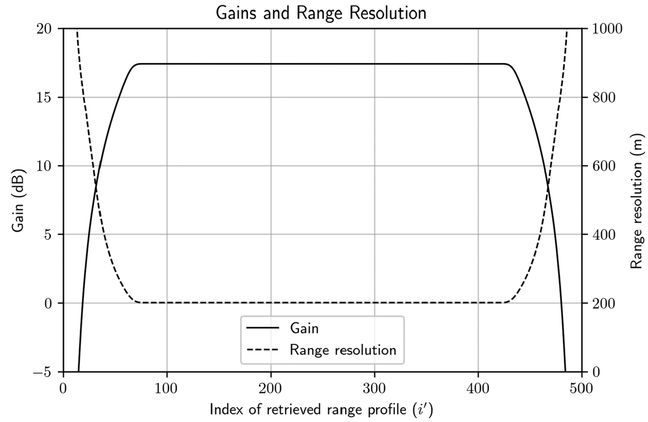

FIGURE 9. **Gain and range resolution of the ZMF, analogous to the results for the standard MF shown in Fig. 7. ZMF enables retrieval in the leading *M* range bins, although the performance in this region remains inferior to that in the central region, which matches that of the standard MF. Performance in the trailing *M* range bins is symmetrically similar to that in the leading edge.**

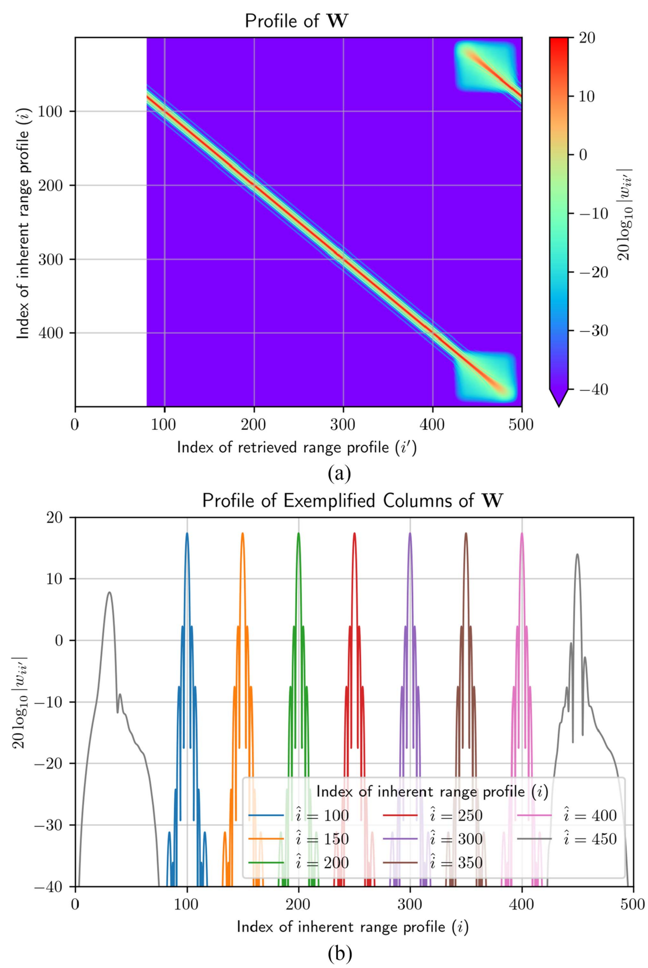

FIGURE 10. **Example of W containing UMF responses across all range bins. This figure corresponds to those for MF and ZMF (see Figs. 6 and 8), but here W is generated using UMF. (a) Full set of UMF responses, where the horizontal axis denotes the indices of the retrieved range profile, $\hat{i}$. (b) Eight selected responses for improved visibility.**

become more significant with longer pulse durations. Moreover, nonlinear chirp and code-modulated waveforms tend to be less tolerant to Doppler shifts. The influence of Doppler can be analyzed through the ambiguity function of a transmitted signal. Although this article does not explore this topic in depth, it has been thoroughly discussed in references such as [1], [22], and [32].

B. WAVEFORMS

The waveform shown in Fig. 2 is a linear up-chirped signal shaped by a raised-cosine window, with roll-in and roll-off times of 10 μs. As shown in Fig. 6, the peak sidelobe level of its MF response is approximately 15.2 dB below the mainlobe peak. It is desirable that the first and several subsequent range sidelobes—including the peak sidelobe—decay more rapidly than the inherent range profiles of weather targets. A straightforward approach is to apply a more aggressive

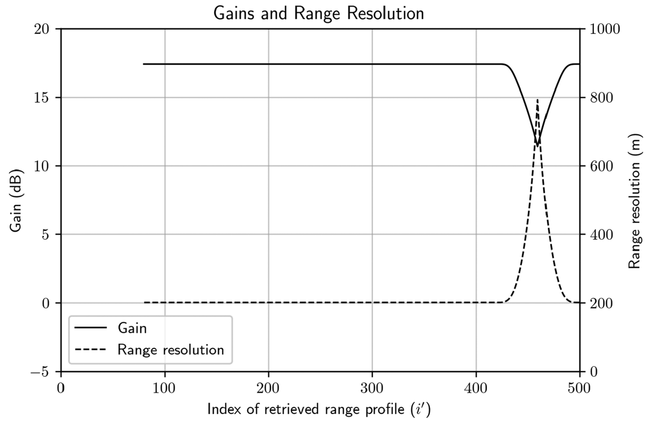

FIGURE 11. Gain and range resolution of the UMF, shown in comparison with the results for MF and ZMF in Figs. 7 and 9, respectively. UMF achieves performance equivalent to MF in terms of gain and resolution but offers a higher sampling rate for the retrieved range profile—eight times higher than that of MF in Fig. 7. The improved range resolution is referred to as display range resolution. Note, however, that UMF enhances only the display range resolution—it does not improve the actual range resolution.

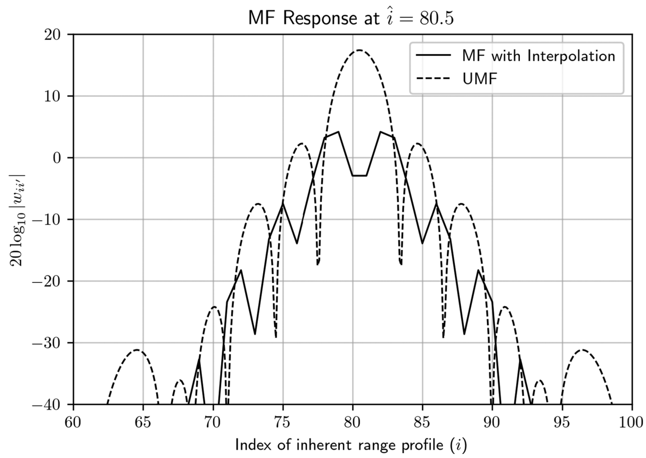

FIGURE 12. Comparison of UMF and interpolated MF responses. While the interpolated MF improves the sampling rate of the retrieved range profile similarly to UMF, its response quality is inferior to that of UMF.

window function, such as the Blackman–Harris window [3]. However, it should be noted that while aggressive windowing reduces sidelobe levels, it also shortens the effective pulse duration and decreases the effective bandwidth of the transmitted signal, causing SNR loss and range resolution degradation. Nonlinear chirp signals offer a way to preserve effective pulse duration [5], [33]. However, like windowed linear chirps, they are affected by reduced effective bandwidth, and their sidelobe levels are practically not as low as those of windowed linear chirp signals [2]. Some studies, such as [18], have successfully designed nonlinear chirp signals with improved performance by optimizing the waveform shapes. Although code-modulated waveforms can provide both wide effective pulse duration and wide bandwidth, they typically exhibit high sidelobes and requires careful consideration of their Doppler tolerance. The properties of these various waveform types have been well documented in [1] and [22].

The appropriate specification of sidelobe requirements for weather radar applications depends on preferences of designers. Nevertheless, a practical criterion—analogous to antenna sidelobe constraints—can be adopted, along with a waveform optimization method designed to satisfy it.

C. FILTERS

Filters other than MF are another means of improving pulse compression performance. Inverse and Wiener filters, such as the MF, are computed based on a transmitted signal replica, and are known for their high-resolution performance, albeit at the cost of reduced SNR [34], [35]. Optimum filters, which are also derived from a transmitted signal, are designed through optimization procedures to achieve specific criteria, such as minimizing the peak sidelobe level or integrated sidelobe level [13], [36]. Adaptive filters, on the other hand, are tailored to each received signal individually. Their responses retain a mainlobe similar to that of MF, while the sidelobe levels are adaptively adjusted based on a range profile of volume targets. In other words, sidelobe suppression is stronger at ranges where strong echoes are received, and weaker where echoes are weak. Adaptive filters, which are still actively studied, can offer the best performance among these methods but require significantly higher computational resources [37], [38]. Furthermore, unlike the other filters, adaptive filters have to be calculated online (in real time), which makes them difficult to be used in practical radars.

VI. SUMMARY

This article began by discussing the technical concept of pulse compression. It was shown that pulse compression radar systems can be regarded as equivalent to conventional radar systems transmitting a waveform shaped like the autocorrelation of the original transmitted signal. This autocorrelation waveform approximates a rectangular pulse whose peak amplitude is enhanced by a factor of $\sqrt{B_r T_e}$, and whose duration is compressed to $1/B_e$, where B_r is the receiver bandwidth, and T_e and B_e are the effective duration and effective bandwidth of the original transmitted signal, respectively.

We then examined how these benefits modify the conventional radar equations for two scenarios: point/hard target detection and volume target estimation. Modified forms—termed pulse compression radar equations—were presented, revealing that pulse compression contributes differently to each application. Specifically, the gain is $B_r T_e$ for a point target and B_r/B_e for a volume target. This difference stems from the fact that volume target radar equations depend on the resolution volume, unlike those for a point target. Using these equations, we also proposed a calibration method based on a reference hard target. Furthermore, we derived SNR expressions for both cases, indicating that they are proportional to T_e and T_e/B_e, respectively, and notably independent of B_r. For a volume target, the effective bandwidth B_e acts as the noise bandwidth rather than the receiver bandwidth.

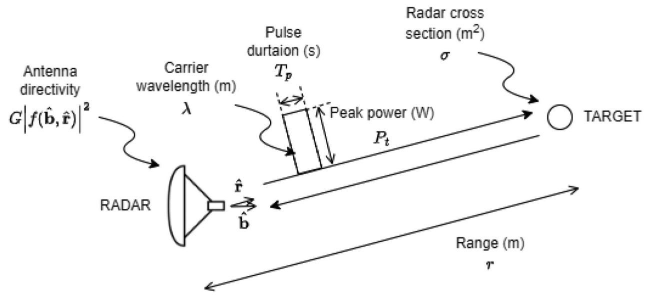

FIGURE 13. Radar observation for a single target with variables of radar equation.

In addition, we introduced practical formulas for estimating the pulse compression-enhanced dynamic range, one for point targets and another for volume targets. To bridge the gap between theoretical analysis and practical digital implementation, we formulated matched filter (MF)—the core of pulse compression—in an explicit digital framework. Two widely used preprocessing techniques, zero-padding matched filter (ZMF) and upsampling matched filter (UMF), were also incorporated and analyzed. Our results confirm that the theoretical performance of MF is preserved under digital implementation, while identifying certain artifacts that arise in practice and are alleviated by the preprocessing steps.

Finally, we briefly discussed related considerations, such as Doppler effects and performance improvements achievable through alternative waveforms and filters. Although these topics are well documented in the literature, their inclusion here completes the practical perspective on pulse compression.

Through this work, we aim to help both new learners and advanced practitioners better understand and utilize pulse compression techniques. We hope that readers not only reproduce its benefits with confidence but also, by referring to the Appendixes, deepen their insight and uncover new perspectives on pulse compression radar systems.

APPENDIX

A. RADAR EQUATIONS

1) POINT TARGET

Fig. 13 illustrates the radar observation geometry and the variables involved in deriving the radar equation. A wave is transmitted from the radar antenna and impinges on the ith target with power (W) given by

$$P_i^{(i)}(t) = P_t \left| a\left(t - \frac{\tau^{(i)}}{2}\right)\right|^2 \frac{G\left|f\left(\hat{\mathbf{b}}, \hat{\mathbf{r}}^{(i)}\right)\right|^2}{4\pi} \frac{1}{r^{(i)2}} \tag{31}$$

where P_t is the peak transmit power (W), and $a(t)$ is the transmit waveform, normalized such that $\max_t |a(t)|^2 = 1$. The variable $\tau^{(i)}$ denotes the round-trip time delay (s) between the radar and the ith target, with the corresponding range given by $r^{(i)} = c\tau^{(i)}/2$, where c is the speed of light (ms^{-1}). The term $G|f(\hat{\mathbf{b}}, \hat{\mathbf{r}}^{(i)})|^2$ represents the antenna directivity pattern where G is the peak antenna gain, $f(\hat{\mathbf{b}}, \hat{\mathbf{r}})$ is the complex antenna pattern, $\hat{\mathbf{b}}$ is the unit vector along the antenna boresight, and $\hat{\mathbf{r}}^{(i)} := \mathbf{r}^{(i)}/r^{(i)}$ is the unit vector pointing from the radar to the target. The antenna pattern is normalized such that $|f(\hat{\mathbf{b}}, \hat{\mathbf{b}})|^2 = 1$, and its integral over the unit sphere satisfies $\int_{-\pi}^{\pi}\int_0^{\pi} G|f(\hat{\mathbf{b}}, \hat{\mathbf{r}})|^2 \sin\theta \, d\theta \, d\phi = 4\pi$, where θ and ϕ are the spherical angular coordinates of $\hat{\mathbf{r}}$ (rad).

The ith target reflects a portion of the incident energy back toward the radar, with returned power (W) given by

$$P_s^{(i)}(t) = P_i^{(i)}\left(t - \frac{\tau^{(i)}}{2}\right)\frac{\sigma^{(i)}}{4\pi}\frac{1}{r^{(i)2}}, \tag{32}$$

where $\sigma^{(i)}$ is the radar cross section (RCS) of the target (m^2), assumed to be sufficiently small compared to the area illuminated by the antenna beam at the range $r^{(i)}$.

The radar antenna then receives the backscattered wave with power

$$P_r^{(i)}(t) = P_s^{(i)}(t)\lambda^2 \frac{G\left|f\left(\hat{\mathbf{b}}, \hat{\mathbf{r}}^{(i)}\right)\right|^2}{4\pi} \tag{33}$$

where λ is the carrier wavelength (m). The term $\lambda^2 G|f(\hat{\mathbf{b}}, \hat{\mathbf{r}})|^2/(4\pi)$ represents the effective aperture area (m^2) of the receiving antenna in the given direction.

Combining (31)–(33), the received signal power from the ith target is

$$P_r^{(i)}(t) = \frac{P_t\left|a(t-\tau^{(i)})\right|^2 G^2 \left|f\left(\hat{\mathbf{b}}, \hat{\mathbf{r}}^{(i)}\right)\right|^4 \lambda^2\sigma^{(i)}}{(4\pi)^3 r^{(i)4}}. \tag{34}$$

This expression shows that the received signal is equivalent to a delayed and scaled version of the transmitted signal. The peak received power from the ith target is then

$$P_r^{(i)} = \max_t P_r^{(i)}(t) = \frac{P_t G^2 \left|f\left(\hat{\mathbf{b}}, \hat{\mathbf{r}}^{(i)}\right)\right|^4 \lambda^2\sigma^{(i)}}{(4\pi)^3 r^{(i)4} l^{(i)2}} \tag{35}$$

where the additional factor $l^{(i)2}$ accounts for power losses in the radar system and wave propagation. Equation (35) is the classic radar equation for point/hard targets, assuming that signals from multiple targets do not overlap significantly.

The SNR is obtained by comparing the received power to the noise power, defined as $P_n = k_B \mathcal{T} B_r$ where k_B is the Boltzmann constant (JK^{-1}), $\mathcal{T}$ is the system temperature (K), and B_r is the receiver bandwidth (Hz). Thus, the SNR is

$$\Pi_r^{(i)} := \frac{P_r^{(i)}}{P_n} = \frac{P_t G^2 \left|f\left(\hat{\mathbf{b}}, \hat{\mathbf{r}}^{(i)}\right)\right|^4 \lambda^2\sigma^{(i)}}{(4\pi)^3 r^{(i)4} l^{(i)2} k_B \mathcal{T} B_r}. \tag{36}$$

2) VOLUME TARGET

A volume target is defined as a dense set of point targets filling a spatial volume. In weather radar applications, it is assumed that numerous hydrometeors are distributed within a volume much larger than the cube of the radar wavelength. This spatial distribution allows the received powers from individual scatterers to be linearly accumulated as

$$
\begin{aligned}
P_r(t) &= \sum_i P_r^{(i)}(t) \\
&= \frac{P_t G^2 \lambda^2}{(4\pi)^3} \sum_i \frac{1}{r^{(i)4}} \left| a\left(t - \tau^{(i)}\right) \right|^2 \left| f\left(\hat{\mathbf{b}}, \hat{\mathbf{r}}^{(i)}\right) \right|^4 \sigma^{(i)}.
\end{aligned} \tag{37}
$$

We now introduce the concept of reflectivity, $\eta(r)$, defined as the backscattering cross section per unit volume (m ^{2} m^{-3})

$$
\eta(r) := \sum_i \frac{\left| a\left(t - \tau^{(i)}\right) \right|^2}{\Delta_r} \frac{\left| f\left(\hat{\mathbf{b}}, \hat{\mathbf{r}}^{(i)}\right) \right|^4}{r^2 \Delta_a} \sigma^{(i)} \tag{38}
$$

where Δ_r is the range resolution (m) and Δ_a is the angular resolution (sr). The range resolution is given by

$$
\Delta_r := \frac{c}{2} \int_0^T |a(t)|^2 \, dt = \frac{cT_e}{2} \tag{39}
$$

where T_e is the effective duration of the transmitted signal, and T is the PRI. The angular resolution is defined as

$$
\Delta_a := \int_{-\pi}^{\pi} \int_0^{\pi} \left| f\left(\hat{\mathbf{b}}, \hat{\mathbf{r}}\right) \right|^4 \sin\theta d\theta d\phi = \frac{\pi \theta_h^2}{8 \ln 2} \tag{40}
$$

assuming a Gaussian antenna pattern modeled as

$$
\left| f\left(\hat{\mathbf{b}}, \hat{\mathbf{r}}^{(i)}\right) \right|^2 = \exp\left(-4 \frac{\theta^2}{\theta_h^2} \ln 2 \right) \tag{41}
$$

where $\cos\theta := \hat{\mathbf{b}} \cdot \hat{\mathbf{r}}$, and θ_h is the half-power beamwidth (HPBW) (rad).

Thus, the reflectivity $\eta(r)$ represents a volume-averaged scattering cross section, where the volume is defined by the radar's range and angular resolutions determined by the signal duration and antenna directivity, respectively. Using this definition, the radar equation for volume targets becomes

$$
\begin{aligned}
P_r(t) &\approx \frac{P_t G^2 \lambda^2}{(4\pi)^3} \frac{\Delta_r \Delta_a}{r^2} \eta(r) \frac{1}{l(r)^2} \\
&= \frac{P_t G^2 \lambda^2 c T_e \theta_h^2}{2^{10} (\ln 2) \pi^2 r^2 l(r)^2} \eta(r)
\end{aligned} \tag{42}
$$

where $l(r)^2$ accounts for system and propagation losses, similarly to (35). The corresponding SNR for a volume target is then

$$
\Pi_r(t) = \frac{P_t G^2 \lambda^2 c T_e \theta_h^2}{2^{10} (\ln 2) \pi^2 r^2 l(r)^2 k_B \mathcal{T} B_r} \eta(r). \tag{43}
$$

B. CORRESPONDENCE BETWEEN REAL AND COMPLEX SIGNALS

Some weather radar systems equipped with IQ demodulators and two ADCs acquire both the in-phase (I) and quadrature (Q) components of received signals [9]. In contrast, many modern radars simplify the hardware by using a single ADC without an IQ demodulator, recording real-valued signals that are later converted to complex form in software. This approach requires real-valued signals to be sampled at twice the rate of their complex counterparts. Enabled by the advent of high-speed ADCs in recent decades, this method avoids several issues associated with analog IQ demodulation, such as gain mismatch, DC offset, and quadrature phase imbalance.

Let $\mathbf{y}_R$ denote a real-valued signal with $2N$ samples. Its corresponding complex-valued signal $\mathbf{y}$ with N samples is given by

$$
\mathbf{y} = \frac{1}{\sqrt{N}} \mathbf{F}^{\mathrm{H}} \mathbf{s} \tag{44}
$$

where $\mathbf{s} = \begin{bmatrix} s_0 & s_1 & \cdots & s_{N-1} \end{bmatrix}^{\mathrm{T}}$ is the complex spectrum of $\mathbf{y}$, computed from the spectrum $\mathbf{s}_R$ of $\mathbf{y}_R$ via

$$
s_n = \begin{cases} \frac{s_{R0} + s_{RN}}{2} + j \frac{s_{R0} - s_{RN}}{2}, & n = 0 \\ s_{Rn}, & n \in [1, N-1]. \end{cases} \tag{45}
$$

The spectrum $\mathbf{s}_R = \begin{bmatrix} s_{R0} & s_{R1} & \cdots & s_{R2N-1} \end{bmatrix}^{\mathrm{T}}$ is obtained by applying the DFT as

$$
\mathbf{s}_R = \sqrt{2N} \mathbf{F} \mathbf{y}_R. \tag{46}
$$

Note that the Fourier matrix in (44) is of size $N \times N$, whereas the one in (46) is $2N \times 2N$.

The inverse transformation from a complex signal back to a real signal is given by

$$
s_{Rn'} = \begin{cases} \mathrm{Re}\left(s_0\right) + \mathrm{Im}\left(s_0\right), & n' = 0 \\ s_{n'}, & n' \in [1, N-1] \\ \mathrm{Re}\left(s_0\right) - \mathrm{Im}\left(s_0\right), & n' = N \\ s_{2N-n'}^*, & n' \in [N+1, 2N-1]. \end{cases} \tag{47}
$$

These forward and inverse transformations exhibit the following three key properties.

1) *Waveform preservation:* The real part of each complex sample corresponds to every other sample of the original real signal as $\mathrm{Re}(s_n) = s_{R2n}$.

2) *Bijective linearity:* The transformations are invertible and linear, establishing a one-to-one correspondence between real and complex signals. No information is lost in the conversion.

3) *Power preservation:* The total signal power is conserved as $\mathbf{s}_R^{\mathrm{H}} \mathbf{s}_R = \mathbf{s}^{\mathrm{H}} \mathbf{s}$.

Equation (45) can be interpreted as applying a Hilbert transform to the real-valued signal to synthesize its imaginary part. The discretized frequency response of the Hilbert transform, $\mathbf{h} = \begin{bmatrix} h_0 & h_1 & \cdots & h_{2N-1} \end{bmatrix}^{\mathrm{T}}$, is defined as

$$
h_{n'} = \begin{cases} 1, & n' = 0 \\ -j, & n' \in [1, N-1] \\ -1, & n' = N \\ j, & n' \in [N+1, 2N-1]. \end{cases} \tag{48}
$$

While this definition preserves all three properties listed above, it differs from the practical approximation commonly used in signal processing textbooks [39], [40], where $h_0 = h_N = 0$ and the remaining $h_{n'}$ are the same as above. This practical form satisfies property 1) (waveform preservation) but sacrifices properties 2) and 3) (bijective linearity and power preservation).

C. RADAR RECEIVED SIGNAL MODEL

Assuming a case where a single pulse is transmitted, the received signal is modeled as

$$\mathbf{y}' = \mathbf{A}'\mathbf{x}' + \mathbf{n}' \tag{49}$$

where the complex received signal is discretized as $\mathbf{y}' := \begin{bmatrix} y_0 & y_1 & \cdots & y_{n'} & \cdots & y_{N'-1} \end{bmatrix}^{\mathrm{T}}$. The sampling interval is denoted as δ_t (s). Since only a single transmission is considered, we assume that N' is sufficiently large for simplicity. The noise vector $\mathbf{n}' := \begin{bmatrix} n_0 & n_1 & \cdots & n_{n'} & \cdots & n_{N'-1} \end{bmatrix}^{\mathrm{T}}$ represents additive noise in the received signal, which is approximately modeled as $\mathbf{n}' \sim \mathcal{CN}(\mathbf{0}, \sigma_n^2\mathbf{I})$. This assumption is valid when $\delta_t \gtrapprox B_r^{-1}$, a condition realizable through appropriate analog and digital filtering at the receiver [41]. The vector $\mathbf{x}' := \begin{bmatrix} x_0 & x_1 & \cdots & x_{i'} & \cdots & x_{I'-1} \end{bmatrix}^{\mathrm{T}}$ represents the (complex) range profile of targets, sampled at an interval $\delta_r := c\delta_t/2$ (m). Here, I' denotes the number of range bins. Its probabilistic model is given by $\mathbf{x}' \sim \mathcal{CN}(\mathbf{0}, \mathrm{diag}(\boldsymbol{\sigma}_{x'}^2))$, where $\boldsymbol{\sigma}_{x'}^2 := \begin{bmatrix} \sigma_{x_0}^2 & \sigma_{x_1}^2 & \cdots & \sigma_{x_{I'-1}}^2 \end{bmatrix}^{\mathrm{T}}$. The matrix $\mathbf{A}'$ is an $N' \times I'$ Toeplitz matrix, illustrated in Fig. 5, whose first column begins with the transmitted signal replica $\mathbf{a} := \begin{bmatrix} a_0 & a_1 & \cdots & a_{M-1} \end{bmatrix}^{\mathrm{T}}$. This replica is normalized such that $\max_m\{|a_m|^2\} = 1$. The duration of the transmitted signal is $M\delta_t$, which is no shorter than its effective time support [see see Fig. 2(a)]. As indicated in Fig. 5, the Toeplitz structure requires $N' = I' + M - 1$.

As discussed previously, radar systems typically discard leading and trailing samples of the received signal. The practically used segment is given by $\mathbf{y} := \begin{bmatrix} y_M & y_{M+1} & \cdots & y_n & \cdots & y_{N-1} \end{bmatrix}^{\mathrm{T}}$, obtained by truncating $\mathbf{y}'$ via

$$\mathbf{y} = \mathbf{T}\mathbf{y}' = \mathbf{T}\mathbf{A}'\mathbf{x}' + \mathbf{T}\mathbf{n}' \tag{50}$$

where the truncation matrix is $\mathbf{T} := \begin{bmatrix} \mathbf{O}_{(N-M)\times M} & \mathbf{I}_{N-M} & \mathbf{O}_{(N-M)\times(N'-2M-N)} \end{bmatrix}$. In this form, $\mathbf{T}$ removes the first M and last $N'-2M-N$ rows of $\mathbf{A}'$. Since the first and last $I'-N$ columns of $\mathbf{T}\mathbf{A}'$ are zero, the product reduces to $\mathbf{T}\mathbf{A}'\mathbf{x}' = \mathbf{A}\mathbf{x}$, where $\mathbf{x} := \begin{bmatrix} x_1 & x_2 & \cdots & x_i & \cdots & x_{N-1} \end{bmatrix}^{\mathrm{T}}$ is a truncated version of $\mathbf{x}'$. Its distribution is given by $\mathbf{x} \sim \mathcal{CN}(\mathbf{0}, \mathrm{diag}(\boldsymbol{\sigma}_x^2))$, where $\boldsymbol{\sigma}_x^2 := \begin{bmatrix} \sigma_{x_1}^2 & \sigma_{x_2}^2 & \cdots & \sigma_{x_{N-1}}^2 \end{bmatrix}^{\mathrm{T}}$. The relationship among $\mathbf{A}'$, $\mathbf{T}\mathbf{A}'$, and $\mathbf{A}$ is visualized in Fig. 5. For the noise term, we define $\mathbf{n} := \mathbf{T}\mathbf{n}'$. It retains the same statistical properties as $\mathbf{n}'$, except for the reduced length: $\mathbf{n} \sim \mathcal{CN}(\mathbf{0}, \sigma_n^2\mathbf{I})$. Therefore, the final form of the received signal model is represented as (23).

D. MATCHED FILTER RESPONSE

In the signal component of the compressed signal, the MF response vector $\mathbf{w}_{\hat{i}}$ equals a scaled and delayed version of the autocorrelation function of the transmitted signal, except for range bins affected by the received-signal truncation. This autocorrelation vector is defined as

$$\boldsymbol{\rho} := \frac{1}{\sqrt{\boldsymbol{\alpha}^{\mathrm{H}}\boldsymbol{\alpha}}}\mathbf{C}^{\mathrm{H}}\boldsymbol{\alpha} \tag{51}$$

where $\boldsymbol{\rho} := \begin{bmatrix} \rho_0 & \rho_1 & \cdots & \rho_{N-M-1} \end{bmatrix}^{\mathrm{T}}$. Accordingly, the pulse compression gain g and the range resolution Δ are defined as

$$g = |\rho_0|^2 = \boldsymbol{\alpha}^{\mathrm{H}}\boldsymbol{\alpha} = \frac{T_e}{\delta_t} \approx B_r T_e \tag{52}$$

where $B_r \approx 1/\delta_t$ holds as in previous sections. The range resolution metric Δ is then given by the energy spread of $\boldsymbol{\rho}$

$$\Delta = \frac{\boldsymbol{\rho}^{\mathrm{H}}\boldsymbol{\rho}}{g}. \tag{53}$$

Alternatively, the resolution can also be expressed in terms of the power spectrum of the transmitted signal. Let $\mathbf{p}$ denote the power spectrum of $\boldsymbol{\alpha}$, defined as

$$\mathbf{p} := \mathrm{diag}\,(\mathbf{F}\boldsymbol{\alpha})^*\ \mathbf{F}\boldsymbol{\alpha}. \tag{54}$$

Then, the resolution can be rewritten as

$$\Delta = \mathrm{length}(\boldsymbol{\alpha})\frac{\mathbf{p}^{\mathrm{T}}\mathbf{p}}{\|\mathbf{p}\|_1^2}. \tag{55}$$

The right-hand side is the ratio of the squared ℓ_2 norm to the squared ℓ_1 norm of the power spectrum, scaled by the waveform length. The vector $\boldsymbol{\rho}$ itself can also be expressed in terms of $\mathbf{p}$ as

$$\begin{aligned} \boldsymbol{\rho} &= \frac{1}{\sqrt{\boldsymbol{\alpha}^{\mathrm{H}}\boldsymbol{\alpha}}}\mathbf{F}^{\mathrm{H}}\mathrm{diag}\left(\sqrt{\mathrm{length}(\boldsymbol{\alpha})}\,\mathbf{F}\boldsymbol{\alpha}\right)^*\ \mathbf{F}\boldsymbol{\alpha} \\ &= \frac{\sqrt{\mathrm{length}(\boldsymbol{\alpha})}}{\sqrt{\boldsymbol{\alpha}^{\mathrm{H}}\boldsymbol{\alpha}}}\mathbf{F}^{\mathrm{H}}\mathbf{p}. \end{aligned} \tag{56}$$

Now (55) can be recast in terms of frequency bin size $\delta_f \triangleq 1/(\mathrm{length}(\boldsymbol{\alpha})\delta_t)$

$$\delta_t\Delta = \frac{\mathbf{p}^{\mathrm{T}}\mathbf{p}\cdot\delta_f}{\|\mathbf{p}\|_1^2\cdot\delta_f^2} = \frac{1}{B_e} \tag{57}$$

since the center term is the reciprocal of a discretized expression of the effective bandwidth. Its continuous counterpart is defined in (2).

Lastly, we examine the noise component of the compressed signal. As defined in (28), it remains a zero-mean complex Gaussian random variable. The variance of its $\hat{i}$th element is

$$\mathrm{E}\left[\left|\hat{n}_{\hat{i}}\right|^2\right] = \frac{\boldsymbol{\alpha}_{\hat{i}}^{\mathrm{H}}\,\mathrm{E}\left[\mathbf{n}\mathbf{n}^{\mathrm{H}}\right]\boldsymbol{\alpha}_{\hat{i}}}{\boldsymbol{\alpha}^{\mathrm{H}}\boldsymbol{\alpha}} = \sigma_n^2 \tag{58}$$

where $\boldsymbol{\alpha}_{\hat{i}}$ denotes $\boldsymbol{\alpha}$ circularly shifted by $\hat{i}$ positions. This shows that the variance of the noise component (after MF) is equal to the variance of the original noise in the received signal (before MF). In other words, MF preserves the noise power due to the normalization factor $1/\sqrt{\boldsymbol{\alpha}^{\mathrm{H}}\boldsymbol{\alpha}}$. Consequently, the pulse compression gain discussed earlier can be interpreted as a gain in SNR.

It is also instructive to consider the case of $B_r \ll 1/\delta_t$, which is practically realized by adopting a high sampling rate. In this regime, the pulse compression gain is given by T_e/δ_t, since the approximation in (52) no longer holds. This expression shows that the gain increases as the sampling rate becomes higher. However, this apparent improvement in gain is offset in terms of SNR, because the noise level after pulse compression increases proportionally to $1/\delta_t$ (while B_r remains unchanged), as indicated by (58).

ACKNOWLEDGMENT

The authors would like to thank Dr. Tomoo Ushio, Professor at Osaka University, and Dr. Jim George, Chief Engineer at the CSU-CHILL National Radar Facility, for their fruitful discussions and valuable insights.

REFERENCES

[1] M. I. Skolnik, *Radar Handbook*, 3rd ed. New York, NY, USA: McGraw-Hill, 2008, pp. 8.1–8.44.

[2] P. Z. Peebles Jr., *Radar Principles*. Hoboken, NJ, USA: Wiley, 1998, pp. 287–354.

[3] T. Mega, K. Monden, T. Ushio, K. Okamoto, Z.-I. Kawasaki, and T. Morimoto, "A low-power high-resolution broad-band radar using a pulse compression technique for meteorological application," *IEEE Geosci. Remote Sens. Lett.*, vol. 4, no. 3, pp. 392–396, Jul. 2007, doi: 10.1109/LGRS.2007.895705.

[4] T. Ushio, E. Yoshikawa, T. Mega, T. Morimoto, and Z.-I. Kawasaki, "Broad band radar for high resolution observation of precipitation," in *Proc. 2008 IEEE Radar Conf.*, Rome, Italy, 2008, pp. 1–5, doi: 10.1109/RADAR.2008.4721126.

[5] J. George, N. Bharadwaj, and V. Chandrasekar, "Considerations in pulse compression design for weather radars," in *Proc. IEEE Int. Geosci. Remote Sens. Symp.*, Boston, MA, USA, 2008, pp. V-109–V-112, doi: 10.1109/IGARSS.2008.4780039.

[6] E. Yoshikawa, T. Mega, T. Morimoto, T. Ushio, and Z. Kawasaki, "Development and observation of the Ku-band broad-band radar for meteorological application," in *Proc. IEEE Int. Geosci. Remote Sens. Symp.*, Boston, MA, USA, 2008, pp. V-578–V-581, doi: 10.1109/IGARSS.2008.4780158.

[7] M. Wada, J. Horikomi, and F. Mizutani, "Development of solid-state weather radar," in *Proc. IEEE Radar Conf.*, Pasadena, CA, USA, 2009, pp. 1–4, doi: 10.1109/RADAR.2009.4977071.

[8] E. Yoshikawa et al., "Rainfall observation with high resolution using Ku-band broad band radar," in *Proc. IEEE Radar Conf.*, Pasadena, CA, USA, 2009, pp. 1–5, doi: 10.1109/RADAR.2009.4977076.

[9] E. Yoshikawa et al., "Development and initial observation of high-resolution volume-scanning radar for meteorological application," *IEEE Trans. Geosci. Remote Sens.*, vol. 48, no. 8, pp. 3225–3235, Aug. 2010, doi: 10.1109/TGRS.2010.2045762.

[10] E. Yoshikawa, S. Yoshida, T. Morimoto, T. Ushio, Z. Kawasaki, and T. Mega, "Initial observation results for precipitation on the Ku-band broadband radar network," in *Proc. IEEE Int. Geosci. Remote Sens. Symp.*, Vancouver, BC, Canada, 2011, pp. 3991–3994, doi: 10.1109/IGARSS.2011.6050106.

[11] T. Ushio et al., "Development of the broadband radar network with high resolution," in *Proc. 30th URSI Gen. Assem. Sci. Symp.*, 2011, pp. 1–4, doi: 10.1109/URSIGASS.2011.6050705.

[12] F. Mizutani, M. Wada, T. Ushio, E. Yoshikawa, S. Satoh, and T. Iguchi, "Development of active phased array weather radar," in *Proc. 35th Conf. Radar Meteorol.*, Pittsburgh, PA, 2011, pp. 1–6.

[13] N. Bharadwaj and V. Chandrasekar, "Wideband waveform design principles for solid-state weather radars," *J. Atmos. Ocean. Technol.*, vol. 29, pp. 14–31, Jan. 2012, https://doi.org/10.1175/JTECH-D-11-00030.1

[14] T. Ushio, E. Yoshikawa, S. Shimamura, Z. Kawasaki, and N. Matayoshi, "Latest observation results of the Ku-band broadband radar (BBR) network project," in *Proc. IEEE Int. Geosci. Remote Sens. Symp.*, Munich, Germany, 2012, pp. 4778–4781, doi: 10.1109/IGARSS.2012.6352545.

[15] E. Yoshikawa et al., "MMSE beam forming on fast-scanning phased array weather radar," *IEEE Trans. Geosci. Remote Sens.*, vol. 51, no. 5, pp. 3077–3088, May 2013, doi: 10.1109/TGRS.2012.2211607.

[16] B. L. Cheong, R. Kelley, R. D. Palmer, Y. Zhang, M. Yeary, and T.-Y. Yu, "PX-1000: A solid-state polarimetric X-band weather radar and time–frequency multiplexed waveform for blind range mitigation," *IEEE Trans. Instrum. Meas.*, vol. 62, no. 11, pp. 3064–3072, Nov. 2013, doi: 10.1109/TIM.2013.2270046.

[17] T. Ushio et al., "Development and observation of the phased array radar at X band," in *Proc. 31st URSI Gen. Assem. Sci. Symp.*, Beijing, China, 2014, pp. 1–4, doi: 10.1109/URSIGASS.2014.6929643.

[18] C. Pang et al., "A pulse compression waveform for weather radars with solid-state transmitters," *IEEE Geosci. Remote Sens. Lett.*, vol. 12, no. 10, pp. 2026–2030, Oct. 2015, doi: 10.1109/LGRS.2015.2443551.

[19] F. Mizutani et al., "Fast-scanning phased-array weather radar with angular imaging technique," *IEEE Trans. Geosci. Remote Sens.*, vol. 56, no. 5, pp. 2664–2673, May 2018, doi: 10.1109/TGRS.2017.2780847.

[20] T. Ushio, E. Yoshikawa, H. Kikuchi, and M. Wada, "Development and observations of the phased array radar for weather application," in *Proc. IEEE Radar Conf.*, Florence, Italy, 2020, pp. 1–3, doi: 10.1109/RadarConf2043947.2020.9266633.

[21] T. Ushio et al., "Recent progress on the phased array weather radar at X band," in *Proc. IEEE Radar Conf.*, New York City, NY, USA, 2022, pp. 1–4, doi: 10.1109/RadarConf2248738.2022.9764164.

[22] A. S. Mudukutore, V. Chandrasekar, and R. J. Keeler, "Pulse compression for weather radars," *IEEE Trans. Geosci. Remote Sens.*, vol. 36, no. 1, pp. 125–142, Jan. 1998, doi: 10.1109/36.655323.

[23] P. Z. Peebles Jr., *Radar Principles*. Hoboken, NJ, USA: Wiley, 1998, pp. 355–375.

[24] V. N. Bringi and V. Chandrasekar, "Dual-polarized radar systems and signal processing algorithms," in *Polarimetric Doppler Weather Radar: Principles and Applications*. Cambridge, U.K.: Cambridge Univ. Press, 2001, pp. 294–377.

[25] V. N. Bringi and V. Chandrasekar, "Scattering matrix," in *Polarimetric Doppler Weather Radar: Principles and Applications*. Cambridge, U.K.: Cambridge Univ. Press, 2001, pp. 45–88.

[26] R. J. Doviak and D. S. Zrnic, "Weather signals," in *Doppler Radar and Weather Observations*, 2nd ed. New York, NY, USA: Dover, 1993, pp. 64–86.

[27] A. V. Oppenheim and R. W. Shaefer, "The discrete Fourier transform," in *Discrete-Time Signal Process.*, 3rd ed. London, U.K.: Pearson, 2010, pp. 623–715.

[28] C. M. Salazar Aquino, B. Cheong, and R. D. Palmer, "Progressive pulse compression: A novel technique for blind range recovery for solid-state radars," *J. Atmos. Ocean. Technol.*, vol. 38, pp. 1599–1611, Sep. 2021, https://doi.org/10.1175/JTECH-D-20-0164.1

[29] C. M. Salazar, B. Cheong, R. D. Palmer, D. Schvartzman, and A. V. Ryzhkov, "Improvements in the compression filter and calibration factor of the progressive pulse compression technique," *IEEE Trans. Geosci. Remote Sens.*, vol. 62, 2024, Art. no. 5101814, doi: 10.1109/TGRS.2024.3353174.

[30] A. V. Oppenheim and R. W. Shaefer, "Sampling of continuous-time signals," in *Discrete-Time Signal Processing*, 3rd ed. London, U.K.: Pearson, 2010, pp. 153–273.

[31] E. Yoshikawa, S. Kida, S. Yoshida, T. Morimoto, T. Ushio, and Z. Kawasaki, "Vertical structure of raindrop size distribution in lower atmospheric boundary layer," *Geophys. Res. Lett.*, vol. 37, 2010, Art. no. L20802, doi: 10.1029/2010GL045174.

[32] R. J. Keeler and C. A. Hwang, "Pulse compression for weather radar," in *Proc. Int. Radar Conf.*, Alexandria, VA, USA, 1995, pp. 529–535, doi: 10.1109/RADAR.1995.522603.

[33] F. O'Hora and J. Bech, "Improving weather radar observations using pulse-compression techniques," *Met. Apps*, 14, 2007, pp. 389–401, doi: 10.1002/met.38.

[34] S. M. Kay, "Least squares," in *Fundamentals of Statistical Signal Processing: Estimation Theory*. London, U.K.: Pearson, 1993, pp. 219–288.

[35] S. M. Kay, "Linear Bayesian estimators," in *Fundamentals of Statistical Signal Processing: Estimation Theory*. London, U.K.: Pearson, 1993, pp. 379–418.
[36] J. E. Cilliers and J. C. Smit, "Pulse compression sidelobe reduction by minimization of L_p-Norms," *IEEE Trans. Aerosp. Electron. Syst.*, vol. 43, no. 3, pp. 1238–1247, Jul. 2007, doi: 10.1109/TAES.2007.4383616.
[37] S. D. Blunt and K. Gerlach, "Adaptive pulse compression via MMSE estimation," *IEEE Trans. Aerosp. Electron. Syst.*, vol. 42, no. 2, pp. 572–584, Apr. 2006, doi: 10.1109/TAES.2006.1642573.
[38] H. Kikuchi, E. Yoshikawa, T. Ushio, F. Mizutani, and M. Wada, "Adaptive pulse compression technique for X-band phased array weather radar," *IEEE Geosci. Remote Sens. Lett.*, vol. 14, no. 10, pp. 1810–1814, Oct. 2017, doi: 10.1109/LGRS.2017.2737032.
[39] R. G. Lyons, "The Discrete Hilbert transforms," in *Understanding Digital Signal Processing*, 3rd ed. London, U.K.: Pearson, 2010, ch. 9.
[40] A. V. Oppenheim and R. W. Shaefer, "Discrete Hilbert transforms," in *Discrete-Time Signal Processing*, 3rd ed. London, U.K.: Pearson, 2010, pp. 942–979.
[41] A. V. Oppenheim and R. W. Shaefer, "Filter Design Techniques," in *Discrete-Time Signal Processing*, 3rd ed. London, U.K.: Pearson, 2010, pp. 963–622.

EIICHI YOSHIKAWA (Senior Member, IEEE) received the B.E. degree in aerospace engineering from Osaka Prefecture University, Sakai, Japan, in 2005, and the M.E. and Ph.D. degrees from Osaka University, Suita, Japan, in 2008 and 2011, respectively.

In 2011, he was a Postdoctoral Researcher with Osaka University and Colorado State University, Fort Collins, CO, USA, and a Postdoctoral Fellow of the Research Fellowship for Young Scientists, sponsored by the Japan Society for the Promotion of Science (JSPS). In 2012, he joined the Japan Aerospace Exploration Agency (JAXA), Mitaka, Tokyo, Japan, where he is currently an Associate Senior Researcher. He is also a Senior Research Scientist with Colorado State University. His research interests include system development, signal processing, and data analysis for weather radar remote sensing and coherent Doppler lidar wind sensing. He has also worked on the practical applications of radar and lidar for both general and aviation weather.

V. CHANDRASEKAR (Fellow, IEEE) received the undergraduate degree from the Indian Institute of Technology Kharagpur, Kharagpur, India in 1981, and the Ph.D. degree from Colorado State University (CSU), Fort Collins, CO, USA in 1986.

He is currently a University Distinguished Professor with CSU as well as an Honorary Distinguished Professor with Finnish Meteorological Institute, Helsinki, Finland. He has made pioneering contributions to weather radar, especially to polarimetric radar, small radar networks for regional deployments and space borne weather radars and more recently phased array weather radars. He has extensive experience in cloud physics, radar system design, radar network development, DSP design, as well as RF communication systems. He has also contributed significantly to radar applications in atmospheric sciences. He conducts research on related topics including machine learning, image processing, and large-scale system simulation. He has organized and participated in many large multiagency, national level experiments involving many radars, aircraft and ground instrumentation. He is an avid experimentalist conducting special experiments to collect in-situ observations to verify the new techniques and technologies. He is currently the Director of the CSU-CHILL radar laboratories and plays an important role in maintaining advanced meteorological radar systems in the world available for research and continues to work actively supporting its research and education mission. He also served as the Research Director of the NSF Engineering Research Center, Center for Collaborative Adaptive Sensing of the Atmosphere (CASA). He serves on the science team of the major international missions, including the NASA TRMM, GPM missions, as well the NASA TEMPEST-D a CubeSat program. He has been very active in outreach programs of radar meteorology, teaching classes and organizing conferences worldwide. He has been the major advisor for more than 50 Ph.D. students. He is a coauthor of three textbooks, *Introduction to Dual Polarization Weather Radar*, *Polarimetric and Doppler Weather Radar* (both by Cambridge University Press), and *Probability and Random Processes* (by McGraw Hill), and five topical books published by the US National Academy.

Dr. Chandrasekar is an elected Fellow of The American Meteorological Society (AMS), American Geophysical union (AGU), Union of Radio Science (URSI), and National Academy of Inventors. He was the recipient of numerous awards, including Knighted by the Government of Finland, the NASA Robert H. Goddard Exceptional Achievement Award, Suomi Technology Medal (from AMS), NOAA/NWS Directors Medal of Excellence, and the IEEE GRSS Distinguished Achievement Award and most Recently the Remote sensing prize from AMS.